Transcriptional dynamics orchestrating the development and integration of neurons born in the adult hippocampus

Natalí B. Rasetto*[,1,2], Damiana Giacomini*[,1,2], Ariel A. Berardino*[,1,3], Tomás Vega Waichman[1,3], Maximiliano S. Beckel[1,3], Daniela J. Di Bella[4], Juliana Brown[4], M. Georgina Davies-Sala[1,2], Chiara Gerhardinger[4], Dieter Chichung Lie[5], Paola Arlotta[#,4], Ariel Chernomoretz[#,1,3], Alejandro F. Schinder[#,1,2]

([1]) Instituto de Investigaciones Biomédicas de Buenos Aires (IIBBA) – CONICET, Argentina

([2]) Laboratory of Neuronal Plasticity, Leloir Institute, Buenos Aires, Argentina

([3]) Laboratory of Integrative Systems Biology, Leloir Institute, Buenos Aires, Argentina

([4]) Dept. of Stem Cells and Regenerative Biology, Harvard University & Stanley Center for Psychiatric Research, Broad Institute of MIT and Harvard, Cambridge, MA, USA.

([5]) Institute of Biochemistry, Friedrich-Alexander Universität Erlangen-Nürnberg, Erlangen, Germany.

(*) equally contributing authors

(#) equally contributing authors

Correspondence should be addressed to: aschinder@leloir.org.ar; achernomoretz@leloir.org.ar; paola_arlotta@harvard.edu

ABSTRACT

The adult hippocampus generates new granule cells (aGCs) that exhibit distinct functional capabilities along development, conveying a unique and dynamic form of plasticity to the preexisting circuits. While early differentiation of adult radial glia-like neural stem cells (RGL) has been studied extensively, the molecular mechanisms guiding the later steps of aGC maturation remain unknown. Here, we used a precise birthdating strategy to follow newborn neurons along their maturation using single-nuclei RNA sequencing (snRNA-seq). Transcriptional profiling revealed a continuous trajectory from RGLs to mature aGCs, with multiple immature stages bearing increasing levels of effector genes supporting neuronal growth, excitability and synaptogenesis. Remarkably, four discrete cellular states were defined by the expression of distinct sets of transcription factors (TFs): quiescent neural stem cells, proliferative progenitors, postmitotic immature aGCs, and mature aGCs. The transition from immature to mature aCGs involved a transcriptional switch that shutdown molecular cascades promoting cell growth, such as the SoxC family of TFs, to upregulate programs controlling neuronal homeostasis. Indeed, aGCs overexpressing *Sox4* or *Sox11* remained stalled at the immature state. Our results unveil precise molecular mechanisms converting adult neural stem cells into functionally integrated neurons.

INTRODUCTION

The hippocampus is involved in processing spatial representations and plays multiple functions in regard to memory acquisition, storage and retrieval [1,2]. The dentate gyrus is the first relay station for signals navigating from the entorhinal cortex to the hippocampus. It bears an architecture with unique dynamics due to the presence of radial glia-like neural stem cells (RGLs), which continuously generate new neurons that integrate in the preexisting networks [3-5]. Such intensive circuit remodeling by adult neurogenesis is crucial for the fine discrimination of similar experiences [6-8]. Adult-born granule cells (aGCs) provide a substrate for the remodeling of perforant-path to GC synapses (dentate input) as well as for mossy fiber to CA3 connections (output) [9-12]. The generation, development, integration, and survival of new aGCs are precisely shaped by the activity and the physiological conditions of local dentate networks. Behaviors that increase the dentate activity such as exercise, environmental enrichment or spatial learning exert positive modulatory effects, while conditions that alter the adult neurogenic niche such as aging, inflammation or neurodegeneration are typically detrimental for neurogenesis [4].

In the mouse brain, developing aGCs express distinct functional characteristics until they become mature after >8 weeks, while in primates this process is thought to last several months [3,13]. The maturation of functional properties over time involve reduction of membrane resistance, expression of voltage-gated channels, afferent and efferent synaptogenesis, switch of GABA-mediated signaling from excitation to

inhibition (**Figure 1A**). At 4 weeks, aGCs display a transient period of enhanced excitability and susceptibility to activity-dependent synaptic plasticity. This period represents a crucial contribution of neurogenesis to circuit remodeling and information processing in the dentate gyrus [9,11,12,14-22]. Once mature, aGCs are similar to GCs born during perinatal development [23,24]. The molecular mechanisms that control the transitions between functional phases in developing aGCs remain unknown.

Recent studies have exploited the power of single-cell transcriptomics to provide comprehensive descriptions of the initial stages of adult neurogenesis, thus identifying RGLs with distinct potential for self-renewal and differentiation [25,26]. Work focused on early phases of adult neurogenesis has strengthened the long-standing notion that RGLs generate intermediate neural progenitor cells (NPCs) with high proliferating capacity. These NPCs progress to early neuroblasts (NB) that would then transition onto a unique immature neuronal state before reaching a mature GC phenotype [27]. Similar conclusions were reached after studying GCs isolated from postnatal and adult mice [28]. However, the entire progression from RGL to a mature aGC has never been studied before.

Here, we put forward the hypothesis that developmental transitions respond to distinctive molecular stages that are sequentially activated in developing aGCs. To optimize the specificity and time resolution of the neuronal population under study, we labeled defined neuronal cohorts at different ages *in vivo* (from 1- to 8-week-old cells) and performed single-nucleus RNA sequencing (snRNA-seq) of isolated aGCs, generating two independent datasets. These datasets displayed high temporal resolution, which enabled us to reveal the profile of immature and mature aGCs. Unsupervised algorithms identified ten clusters that assembled into a linear developmental trajectory. This continuous pathway was reflected in the transcriptional dynamics of effector genes including pathfinding and cell-adhesion molecules, ion channels, neurotransmitter receptors, and components of the synaptic machinery. Pseudotime analysis revealed four distinct cell states: RGLs, NPCs, immature-, and mature aGCs. The molecular transition from immature to mature aGCs involved a notable switch in the expression of transcription factors (TFs) and their target genes. The shutdown of *SoxC* genes emerged as a crucial event to complete the maturation process. Supporting this hypothesis, overexpression of *Sox4* or *Sox11* maintained developing aGCs in a persistent immature phenotype. Our work uncovers the transcriptional dynamics governing morphological and functional development of GCs in the adult hippocampus.

RESULTS

Transcriptomic profiling of adult neurogenesis with high temporal resolution

To profile neurogenesis in the adult mouse hippocampus, we utilized a strategy to isolate developing cells derived from RGLs expressing the proneural gene *Achaete-scute homolog 1* (*Ascl1*) [25,29,30]. Tamoxifen

administration to young-adult *Ascl1*^{CreERT2};*CAG*^{floxStopSun1sfGFP} mice were used to induce the expression of Sun1-sfGFP in the nuclear membrane of RGLs and permanently label their progeny (**Figures 1B and S1A**) [31]. This birthdating tag enabled a comprehensive analysis of the entire process encompassing neuronal differentiation, development, and functional maturation. A first dataset was built using FACS-sorted nuclei obtained from dentate gyri microdissected at 1-, 2-, 4-, and 8 weeks after induction (cohorts *w1* through *w8*). High-throughput snRNA-seq carried out using Chromium 10X Genomics 3' end sequencing technology rendered 14,367 profiles with a median of 2,994 genes/nucleus belonging to all four cohorts (**Figure S1B-E**). Plotting dataset 1 using t-distributed stochastic neighbor embedding (*t*-SNE) revealed that nuclei from the distinct cohorts formed a continuous sequence organized by neuronal age (**Figure 1C**). Considering a mutual k-nearest neighbor graph (mKNN, k=40), we used a graph-based unsupervised (Louvain) clustering procedure to group nuclei into communities. This initial graph-based partition was further refined and revealed 13 clusters [32] (**Figure 1D**). Clusters #1 through #10 seemed to constitute a linear developmental trajectory, while clusters #11, 12 and 13 appeared separated from each other and distant from the main pathway. All clusters displayed individual signatures that supported the definition of the unsupervised partitions (**Figure 1E**). The identity of each cluster was determined by the expression of canonical markers. The majority of cells (about 88% of dataset 1) were distributed in partitions #3 through #10 that belonged to the neuronal lineage and were identified by the expression *Rbfox3* (*NeuN,* panneuronal marker), *Prox1* (aGCs), and doublecortin (*Dcx,* immature neurons; **Figure 1F**). Although astrocytes (cluster #1) and RGLs (#2) are known to be transcriptionally similar, astrocytes were defined by the restricted expression of *Gfap* and *Slc7a10,* together with *Slc1a2, HopX* and *Notch2* that were also expressed in RGLs [28,33].

Clusters #11, 12, and 13 encompassed non-neuronal cells that are not described as *Ascl1*$^{+}$ lineage [29]. These groups included pericytes expressing *Tbx18* and *Slc6a13* (#11), oligodendrocytes expressing *Mag* and *Mog* (#12), and oligodendrocyte precursor cells expressing *Prkg2* and *Cspg4* (#13). Their scarce representation in the entire dataset (<2%) and their separation from the developmental trajectory suggested a transient expression of *Ascl1* in these cell types not related to neurogenesis.

Both the *t*-SNE and mKNN graphs indicated that aGCs follow a linear developmental trajectory encompassing nine stages (**Figure 2A**). While unsupervised clustering relied entirely on genetic profiles, nuclei followed a linear track ordered by neuronal age in the mKNN graphs (**Figures 2C,D and S1F**). Clusters belonging to the neuronal lineage (*Rbfox3*$^{+}$*, Prox1*$^{+}$) followed a linear sequence containing neural progenitor cells (NPCs), neuroblasts (NB1, NB2), immature neurons (GCimm1, GCimm2), young neurons (GCyoung), and mature GCs (GCmat1, GCmat2). NPCs were recognized by the expression of *Eomes, Top2a,* and *Nell3*, *Cdk6, Lockd, Mcm6,* and *Pola1*, revealing active cell cycle activity (**Figures 2B and S4A**)**.** Interestingly, the presence of *Elavl2, Igfbpl1, Sox4* and *Sox11* revealed that neuronal commitment has already occurred in this early state. Neuroblasts lacked genes involved in cell cycle and expressed immature neuronal markers including *Dcx, Calb2, Rgs6, Sox11, Tac2 and Sox4*. GCimm1 and 2 shut down *Calb2 and Elavl2*, and expressed *Dcx,*

Sox11, Igfbpl1, Rgs6, Camk4, and Chd5. Interestingly, GCyoung showed diminished expression of immature neuronal markers and enhanced levels of *Calb1, Icam5, Tenm1,* and *Grin2a.* The final maturation stages GCmat1 and 2 had completely shut-off immature markers and expressed *Ntng1*.

The cohort analysis allowed to define the time course for cluster onset (**Figures 2D and S1F**). Thus, RGLs were detected at early timepoints and declined sharply in w8, in line with the limited proliferative capacity and self-renewal of *Ascl1*-expressing stem cells [25,30]. NPCs were scarce, as expected based on their fast division and rapid differentiation, and mostly present in w1 and w2. Neuroblasts were distinguished by their early onset and rapid disappearance, particularly NB2. Immature and young neurons appeared sequentially with distinctive temporal progression. GCimm1 was primarily emerged in w1 and reached a maximum in w2, while GCimm2 was observed in w2 and w4. GCyoung was uniquely found in w4, which strongly suggests that this cluster corresponds to developing aGCs undergoing their critical period of enhanced plasticity. Mature aGCs (GCmat) were primarily observed in w8. Although dataset 1 revealed important changes in cluster composition from w2 to w4 and w8, additional transitions occurring at intermediate times might have been oversighted. To improve time resolution, we collected dataset 2 with cohorts at 2, 3, 4, 5, and 8 weeks (w2 through w8; **Figures S2A,B**). After assessing for the biological reproducibility between both datasets we used Seurat functionality to transfer the cluster labels from dataset 1 to nuclei from dataset 2 (**Figures S2C,D;** see Methods). Clusters in dataset 2 maintained overall properties including differentially expressed genes through transitions, timing of appearance of the distinct clusters, and expression of canonical markers, although with a somewhat slower pace (**Figures S2E,F and S3**). None of the nuclei of dataset 2 was assigned as NB2, probably due to the fact that the dataset did not include a timepoint at 1 week. GCyoung was again dominant in w4, GCmat1 was again maximally expressed at w8, but it was also present at w5, suggesting an earlier onset.

This analysis describes the continuous trajectory of a unique neuronal type, the adult-born granule cell, through distinct developmental stages from RGL to GCmat**.** These multiple intermediate transient stages exhibited at the transcriptomic level denote higher complexity than the predicted from functional studies, and establishes the molecular basis for the morphological and physiological changes occurring during aGC development.

Effector molecules building neuronal function are expressed in the immature clusters

The pathway from RGL to NPC and then NB1 involves profound cell biological transitions, from a quiescent to a proliferating state, and then to postmitotic neuron. We found that these transitions displayed the highest numbers of differentially expressed genes (DEGs), particularly in terms of transcript shutdown (**Figures 2E and S3B**). The RGL to NPC transition included about 200 genes that became silenced thereafter, shutting down a pluripotent program and entering a mitotic phase (**Figures 3A,B**). NPCs were the only dividing cell state, expressing multiple cell-cycle genes and displaying an early neuronal commitment revealed by the

expression of *Eomes, Sox4, Sox11* and *Igfbpl1* (**Figures 2B and S4A**). The trajectory was followed by two types of neuroblasts, NB1 and NB2, lacking cell-cycle genes but with maximal levels of *Dcx* and *Igfbpl1* expression (**Figure 3C**). The transition from NPC to NB1 upregulated transcripts controlling neuronal differentiation and morphogenesis, cell-cell interaction, development and guidance of neuronal projections and synaptic organization (**Figure 3D**).

Canonical markers of early neuronal development including *Dcx*, *Sox4*, *Sox11*, *Igfbpl1* and *Rgs6* were expressed within a restricted segment of the trajectory, from NB1 until GCimm2 (**Figures 2B and S3A**). Transitions from neuroblast to GCimm2 primarily involved upregulated gene expression with few downregulated transcripts, suggesting that developing aGCs continued to incorporate molecules that expanded their structural and functional capabilities (**Figures 2E and S3B**). In general, effector genes that showed an onset of expression in NB1 increased steadily and were maintained until maturation (**Figure 3C**). This was the case for genes related to synaptic transmission such as *Cacna1e, Camk4, Cdh8, Fgf14, Gabrb1, Gabrg3, Grin2a, Grm5, Grm7, Kcnma1* and *Syt1* (**Figure 4**). A fraction of the genes upregulated in NB1 were only expressed in immature neurons (**Figure S4B,C**). The transition from NB1/NB2 to GCimm1 displayed a marked increase in GABA and glutamate receptor subunits, voltage-gated ion channels and cell-adhesion molecules, among the multiple transcripts supporting neuronal function. Other genes involved in axon guidance such as *Robo1, Nrp1, Epha7, Dscam, Ncam2, Epha6, Slit3, Ptpro* displayed an expression that was restricted to immature stages (**Figure 4B,C**).

NB2 constituted a parallel pathway diverging from NB1 towards GCimm1. In the progression from w1 to w2, the NB2 population dropped twice as fast as NB1, suggesting a shorter half-life (**Figure 2D**). The canonical marker for the neuroblast stage *Calb2* was mainly present in NB2, similarly to *Tac2* and *Rgs6* (**Figure 2B**). Compared to NB1, NB2 displayed about 50 additional transcripts with almost no reduction in gene expression (**Figures 2E and 3E**). Some of those transcripts continued to increase in subsequent clusters (GCimm1 and 2), such as *Grin2a, Grid1* and *Grip1* involved in the assembly of glutamate receptors; *Robo2, Sema3c* and *Unc5d* participating in axon guidance; and *Ephb1, Cdh4, Pcdh7, Nrxn3* responsible for cell-cell interaction (**Figure S4D**). These findings suggest that NB2 might be at a more advanced developmental stage, closer to GCimm1 than NB1.

GCimm1 and GCimm2 shared specific markers that were previously described for immature GCs [28] (**Figure S5A,B**). Some of these markers, *Adamst18, Nell1, Sema3c* and *Robo1,* were validated by fluorescence *in situ* hybridization (**Figure S5C**). Their expression was confined to the inner granule cell layer, the area where immature aGCs are typically found [34,35]. Besides these general similarities, GCimm2 displayed a distinct profile indicating a more advanced developmental stage, including genes related to synapse formation and plasticity, such as *Camk2a* and multiple glutamate receptor subunits: *Grm1*, *Grid1*, *Gria3*, *Grin2a*, *Grm5* and

Grm7 (**Figure 4B,C**)[36-38]. These findings suggest that GCimm2 initiates a program for glutamatergic synaptogenesis, which has typically been shown in electrophysiological studies in 2-week-old aGCs.

The transition from GCimm2 to GCyoung revealed a major switch that marked the end of the immature period (**Figures 2E and 5A,B**). Multiple transcripts that had reached maximal expression during early development, shut down in GCyoung: *Adamts18, Dcx, Hcn1, Igbpl1, Robo1, Rgs6, Sema3c, Sema3e, Sox4, Sox11*. The GCimm2 to GCyoung transition exhibited a large number of DEGs, highlighting the complexity required to complete neuronal maturation. To better understand the functional changes involved in this transition, we performed enrichment analysis of GO terms (**Figure S6**). Biological processes related to axonal growth and development shut down, while postsynaptic organization, transmission and plasticity appeared during this transition. Furthermore, GCyoung showed plateau levels in typical effector genes related to excitability and neurotransmission (**Figure 4D**). These transcripts included the vesicular glutamate transporter VGLUT1 (*Slc17a7*), the K+/Cl- cotransporter KCC2 responsible for the GABA switch (*Slc12a5*), and *Camk2a* and *Grin2a*, crucial for synaptic plasticity (**Figure 5B**).

The early clusters described above, RGL, NPC and neuroblasts, reflect different cellular stages that bring neural stem cells towards postmitotic neuronal differentiation. From the neuroblast stage onwards, developing aGCs incorporate molecules that expand their functional capabilities, with little transcript shutdown. The transition to GCyoung involves a major change in the transcriptomic profile supporting the ability to release glutamate, exhibit increased excitability, and synaptic plasticity. These features are entirely consistent with prior electrophysiological characterizations of hyperexcitable four-week-old aGCs [14-16,18,20].

The final step to GCmat1 maintains a similar profile with increased expression levels

The GCyoung and GCmat1 clusters were observed at the w4 and w8 timepoints, respectively, which is coincident with the interval at which aGCs become functionally mature [3]. The GCyoung to GCmat transition was characterized by a few DEGs with subtle changes in their expression level (**Figure S7A,B**). A small group of the DEGs constituted markers of GCmat1: *Car10, Chst9, Inpp4b, Ntng1, and Rapgef5*. Other genes were specifically downregulated in GCmat1: *Lin7a*, *Meg3*, *Pcdh15, Plppr1*, and *Slc8a1* (**Figure 5C**). Notably, a subgroup of cells that expressed genes compatible with a ventral localization, which is associated to different functional properties, was only found in these two clusters (**Figure S7C**)[39,40]. Notably, the GCyoung and GCmat1 clusters display similar expression profile but distinct function, suggesting that physiological maturation is also influenced by additional factors other than their transcriptomic signature. The high similarity between these clusters suggests that the GCyoung stage is the early phase of a maturation process that gets consolidated over time.

GCmat2 was a small but sharply defined cluster that contained cells belonging to cohorts w4 onwards in both datasets, and exhibited a large proportion of DEGs when compared to GCmat1 (**Figure 2E**). GCmat2 displayed a set of well-defined markers whose expression in the granule cell layer has been linked to activity: *Acvr1c, Sorcs3, Nrxn3,* and *Kcnip3,* among others [41] (**Figure 5D**). Moreover, *Bdnf*, a neurotrophin whose synthesis and secretion depend on neuronal activity, was only expressed in this partition [42,43]. Despite being a marker for immature neurons, *Rgs6* expression has been reported to increase in aGCs after running, and it is also upregulated in GCmat2 (**Figure 2B**) [44]. To confirm this activity-dependent signature, mice were exposed to enriched environment for 2 days, a condition that increases neuronal activity in the granule cell layer [45]. This stimulus resulted in a marked increase in the expression of the *Acvr1c* receptor monitored by immunofluorescent *in situ* hybridization (**Figure 5E**). Therefore, GCmat2 was classified as a cluster containing neurons belonging to the w4–w8 timepoints that were likely to be electrically active before isolation.

A transcriptional switch underlying neuronal maturation

Based on the extent of differential gene expression, we defined three critical transitions: RGL to NPC, NPC to NB, and GCimm2 to GCyoung. To better understand the molecular principles guiding this process, we analyzed the profile of TF expression. Aligning TFs in accordance to their expression onset or shut-off revealed four distinct signatures that were readily observed in the resulting heatmaps: one containing RGLs, another for NPCs, a longer window encompassing all immature neurons (NB1 through GCimm2), and a last interval including GCyoung and GCmat1 (**Figure 6A,B**). TF expression displayed different patterns, with a majority restricted to the RGL cluster (such as *Etv4, Etv5, Tcf7l1, Hes5, Gli1*), others remaining in NPCs (*Ascl1, Sox6, Sox9, Gli2, Fezf2*), some covering only the NB stage (*Emx1, Klf3, Zhx3*). Multiple TFs encompassed the trajectory from NB to GCimm2, including *Sox4*, *Sox11*, *Tbr1*, *Bach1*, and *Klf12,* while others remained silent through development to became expressed in GCyoung (*Atf6, Runx2, Mkx* or *Foxk1*). Interestingly, a subset of TFs expressed in RGLs shut down in NPCs and were upregulated in GCyoung and GCmat1. This was the case for *Foxo1, Glis3, Bcl6* and *Hlf*.

We assigned pseudotime values to all nuclei along the continuous differentiation trajectory from RGL to GCmat1 (**see Methods section**) and organized the datasets to obtain one density plot for each cohort (**Figures 6C and S8A**). Pseudotime plots displayed four distinct peaks separated by clear valleys that strengthened the distinct signatures defined by the TF analysis. With these data we defined four cellular states: one state corresponding to RGLs, another one containing NPCs, a third state enclosing immature neurons from NB1 to GCimm2, and a last one containing GCyoung and GCmat1. These profiles highlighted crucial transitions in the developmental landscape. Cell clusters within each state display progressive changes in the expression level of effector genes with little modifications in TFs. Differences among states reflect a significant departure from previous features, involving radical switches in TF expression.

The first two transitions reflect distinct cellular states: entering mitosis, then becoming postmitotic, the pathway from a stem cell to a neuron. In contrast, the third transition occurs within different states of that same neuron: an immature aGC becoming mature. To better understand the biological significance of this process, we evaluated the expression of TFs and their target genes (regulons) corresponding to the third and fourth cellular states, aiming to identify master regulators for this final step in the developmental trajectory. This analysis (performed using *SCENIC,* see Methods) revealed >20 regulons displaying selective expression in the third state, with highest levels for the *SoxC* family genes *Sox4* and *Sox11.* Regulons present in the fourth state included high levels of *Foxo1*, *Atf6*, *Klf9*, *Tef*, *Hlf*, and *Glis3* (**Figures 6D and S8B**). Remarkably, all of these TFs have been shown to control signaling pathways regulating neuronal homeostasis [46-50]. *Sox4* and *Sox11* have been shown to play a critical role in early differentiation and neuronal growth, both during perinatal development and in adult neurogenesis [51,52]. However, their participation during late neuronal maturation remains unknown. The shutdown of these *SoxC* TFs in the last neuronal state suggested two possibilities: 1) they are not needed for the final transition and their downregulation results as a secondary effect of a global transcriptional program; 2) their absence might be required for developing neurons to transition to a mature stage.

To discriminate between these possibilities, we investigated the effect of the sustained expression of *Sox4* or *Sox11* on aGC development. RV-Sox4-GFP or RV-Sox11-GFP were delivered to the dentate gyrus of adult mice to infect mitotic NPCs, coincident with the onset of endogenous expression of *Sox4* and *Sox11*. The impact of TF overexpression in the neuronal progeny was studied after 5 weeks, at which time new aGCs become mature. As revealed by immunofluorescence imaging, the immature neuronal marker *Dcx* was absent in control aGCs but it was observed in >60-80% of neurons overexpressing Sox4 or Sox11, suggesting that cells failed to downregulate DCX upon Sox4/11 overexpression (**Figure 7A-C**). In addition, electrophysiological recordings in acute hippocampal slices showed that aGCs overexpressing *Sox11* displayed high membrane resistance and excitability, as well as impaired capacity to fire repetitive action potentials (**Figure 7D-H**). Together, these results indicate that aGCs with sustained expression of Sox4 or Sox11 maintain immature features [53,54]. We therefore conclude that shutdown of *SoxC* TFs is a necessary condition for developing aGCs to become mature.

DISCUSSION

New aGCs develop and integrate in a preexisting network, adding plasticity to the circuitry. The molecular basis of this complex form of circuit remodeling have remained largely unknown. Previous work has captured aspects of adult neurogenesis by means of transcriptomic profiling with a focus on the early molecular cascades underlying the differences between quiescent and active RGLs, and NPCs [26,55]. Subsequent work has

conveyed the notion of a linear trajectory reaching the early neuroblast stages [27]. More recently, a study reported similar transcriptional profiles for immature GCs obtained from the perinatal, postnatal and adult hippocampus [28]. In this work we performed a comprehensive analysis of the entire process encompassing differentiation, development, and functional maturation of aGCs. The strategy involved the initial analysis of cohorts of aGCs at 6 timepoints that allowed us to assign precise time stamps to distinctive and key transitions along the developmental trajectory. In general, the dynamics and gene expression profiles matched very closely previous descriptions of developing aGCs obtained with immunohistochemical, morphological and electrophysiological approaches. These datasets now provide a thorough molecular description of intermediate and end states underlying neuronal development in the adult hippocampus, assigning specific transcriptomic profiles to the individual stages, revealing TFs controlling the process and the effector molecules that convert those programs into neuronal function.

The different phases of adult neurogenesis were previously characterized by the expression of stage-specific markers defined by immunolabeling. Thus, RGLs gave rise to NPCs and, subsequently, to neuroblasts that were thought to keep limited proliferative capacity [56,57]. Our results reveal that NPCs are the only mitotic stage in aGC development, and neuroblasts are committed postmitotic neurons [28]. Two types of neuroblasts were observed: NB1 arising from NPCs, and NB2 shedding from NB1, forming a parallel pathway reaching GCimm1. *Rgs6* was upregulated in NB2 and continued to be expressed until GCimm2, which suggests that NB2 might be a more advanced stage of maturation [44]. The immature neuronal stages GCimm1 and GCimm2 were composed mostly of 2- to 4-week-old cells and expressed immature neuronal markers. The more advanced cluster (GCimm2) showed the upregulation of >100 genes, including those related to the onset of glutamatergic synaptogenesis, known to occur by the second developmental week [34,58-60]. This finding indicates that GCimm2 may be the molecular transition that accompanies the onset of glutamatergic connectivity.

Approaching the GCyoung stage involved substantial profile changes (250-350 DEGs in both datasets) that were only comparable in magnitude to the transitions from RGL to NPC, and NPC to NB1. Multiple effector genes reached plateau levels at GCyoung, including those required for neurotransmission and plasticity, from the presynaptic vesicular glutamate transporter (*Slc17a7*) and vesicular release (*Syt7*) to postsynaptic glutamate and GABA receptors. Because GCyoung contained predominantly w4 cells, we propose that aGCs in this cluster correspond to 4-week-old aGCs with enhanced excitability and synaptic plasticity, described extensively in the literature [14-16,18,20,59]. Despite containing the fundamental building blocks required for neuronal function, 4-week-old GCs are not yet mature. In fact, mature aGCs (>8 weeks) exhibit maximal glutamatergic synaptic strength, overall maturation of GABAergic inhibition, and reduced excitability [18,53,61,62]. Few transcripts were found to be selectively upregulated or downregulated in the

transition from GCyoung to GCmat1, suggesting that the GCyoung cluster is the early phase in a final step of maturation that becomes consolidated over time.

Analysis of DEGs and TFs expression predicted three critical transitions, which were subsequently confirmed by pseudotime analysis. These transitions demarcate four cellular states: RGL, NPC, immature neurons (NB1 to GCimm2), and a mature state (GCyoung and GCmat). Regulon analysis revealed TF networks dominating the immature and mature states **(Fig 6D).** *Sox4* and *Sox11* regulons resulted with the highest specificity scores in the immature state, posing them as critical organizers of the regulatory network. These TFs were known to be involved in the early steps of differentiation during perinatal and adult neurogenesis [51,52]. Our results demonstrate that shutdown of SoxC TFs is a critical mechanism required for neuronal maturation.

Regulons dominating the fourth state included *Foxo1, Klf9, Hlf, Tef,* and *Atf6*, among others. We have hypothesized that these TFs might drive developing aGCs towards a homeostatic state required for maturation. For instance, Foxo family TFs have been recently shown to be critical for autophagy, neuronal migration, growth, and connectivity [47]. Klf9 was also shown to limit excitatory input connectivity in mature aGCs [48]. Neuronal cultures lacking Hlf and Tef by genetic ablation were shown to display disproportionate upregulation of input excitation when deprived of activity, pointing to their central role in the homeostatic regulation of neuronal connectivity [49]. Atf6 is has been associated with calcium homeostasis in models of endoplasmic reticulum stress and Huntington´s disease [46,63]. Finally, Glis3 has been associated also with autophagy and control of neuronal growth and complexity [50]. Foxo1, Atf6, Tef and Mkx regulons share a common downstream TF, Hivep2 (Schnurri-2). Remarkably, dentate gyrus GCs from mice lacking this TF displayed overall altered morphology [64]. In light of these results, our findings support the hypothesis that the transcriptional switch occurring from the immature to the mature neuronal states awakens multiple pathways to exert a tight control of neuronal growth, connectivity and homeostasis. The data presented here opens a new scenario to unravel the temporal dynamics involving master transcriptional regulators that control neuronal maturation in the healthy adult brain, and will serve as the basis to identify mechanisms contributing to aberrant circuit remodeling in brain disorders.

ACKNOWLEDGMENTS

We thank members of the A.F.S., A.C., and Emilio Kropff labs for insightful discussions, and Mariela Trinchero for critical comments on the manuscript. D.G., A.C. and A.F.S. are investigators in the Consejo Nacional de Investigaciones Científicas y Técnicas (CONICET). N.B.R, A.B. and M.B. were supported by CONICET fellowships. This work was supported by grants from the National Institute of Neurological Disorders and Stroke (NINDS, R01NS128117) to P.A., NINDS and Fogarty International Center (FIC) (R01NS103758) to A.F.S.

and P.A., and the Argentine Agency for the Promotion of Science and Technology (PICT 2017-0389) to D.G., (PICT 2018-03713) A.C., and (PICT-2020-0046 and PICT-2021-0077) A.F.S.

MATERIALS AND METHODS

Animals

Male and female C57Bl/6J wild type and genetically modified mice (6–8 weeks of age) were housed at four to five mice per cage in standard conditions. For adult neurogenesis snRNA-seq experiments, *Ascl1*^{CreERT2} (*Ascl1*$^{tm1(Cre/ERT2)Jejo/J)}$) mice were crossed to *CAG*$^{floxStop\text{-}Sun1/sfGFP}$ (B6.129-*Gt(ROSA)26Sort*$^{m5.1(CAG\text{-}Sun1/sfGFP)Nat/MmbeJ}$) conditional reporter line to generate Ascl1^{CreERT2};CAG$^{floxStop\text{-}Sun1/sfGFP}$ mice, which were used to reliably target adult-born GC nuclei [30,31,65]. Tamoxifen (TAM) induction (120 µg/g, four injections in two consecutive days) resulted in the expression of Sun1-sfGFP in the nuclear envelope of Ascl1^{+} cell progeny. Mice were anesthetized (150 µg ketamine/15 µg xylazine in 10 µl saline per g) and sacrificed at the indicated times after TAM induction: 1-, 2-, 4- and 8 weeks for dataset 1, and 2-, 3-, 4-, 5- and 8 weeks for dataset 2. Mice were maintained in C57BL/6J background. Experimental protocols were approved by the Institutional Animal Care and Use Committee of the Leloir Institute, according to the Principles for Biomedical Research involving animals of the Council for International Organizations for Medical Sciences and provisions stated in the Guide for the Care and Use of Laboratory Animals

Tissue dissection

Mice were deeply anesthetized (ketamine/xylazine, as described above), brains were carefully removed and placed into ice cold Earl's balanced salt solution (EBSS, in mM: 117 NaCl, 5.4 KCl, 1 NaH_2PO_4, 26 $NaHCO_3$, 5.6 glucose, 1.8 $CaCl_2$.$2H_2O$ and 0.8 $MgSO_4$) with trehalose 5% v/v and kynurenic acid 0.8 mM [66]. Dissection solution was equilibrated in 95% O_2/5% CO_2 before use. The brain was cut along the longitudinal fissure and the regions posterior to lambda were cut off. Under a dissection microscope and upon removal of the diencephalon, the medial side of the hippocampus was exposed. The dentate gyrus was isolated by inserting a sharp-needle tip and sliding it superficially along the septotemporal axis of the hippocampus. The dissected tissue was placed in a 0.5 ml microcentrifuge tube with a minimal amount of media, flash-freezed on dry ice and stored at -80°C until use.

Nuclei isolation and FACS sorting

Nuclei were isolated as previously described with several modifications [67]. Dounce tissue grinder and pestles were sequentially washed with 100% EtOH, RNAse Zap (Sigma, Cat # R2020), 2-3 rounds with RNAse-free water, and finally rinsed with EZ Lysis Buffer (Sigma, Cat # NUC-101). All material and buffers were chilled on ice. The tissue was transferred to a chilled dounce prefilled with 2 ml ice-cold EZ Lysis Buffer and homogenized slowly with 20-25 strokes of pestle A, followed by 20 strokes with pestle B. Suspension was transferred to a chilled tube and incubated on ice 5 min. Then the suspension was centrifuged at 500 × g for 5 min at 4°C and the supernatant was removed. The pellet was resuspended in 4 ml ice-cold EZ Lysis Buffer and after a second round of ice incubation and centrifugation, the isolated nuclei were resuspended in 4 ml

ice-cold Nuclei Suspension Buffer (NSB) (1x RNase-free molecular-biology grade PBS, 0.1% molecular-biology grade BSA 100 µg/ml and 0.2U/µl RNase inhibitor). Finally, nuclei were centrifuged at 500 × g for 5 min at 4°C and after removing the supernatant were resuspended in 1ml NSB-Ruby (final Ruby concentration 1:500) and filtered twice through a 35-µm cell strainer to remove as many debris as possible. Nuclei were kept on ice until sorting (Harvard University, Bauer Core Facility, BD FACSAria II) into 96 well plates, pre-coated with BSA to reduce adherence and improve recovery, containing with ~10-20 µl of rich-NSB (with final 2U/µl of RNase inhibitor and 1% BSA). The final nuclei concentration was determined using a C-chip Neubauer counting chamber and Trypan Blue (1:2 final dilution). Nuclei were immediately loaded for single-cell GEM formation (10x Genomics, single cell RNA sequencing 3', Chromium v3.1).

10x Genomics Chromium

Dataset sampling for snRNA-seq experiments was carried out within a minimal time interval, processing two time points in a single experiment each day to minimize batch effects. For each time point, four dentate gyri (left hemispheres) from male and female mice were pooled. If needed to increase nuclei number, dentate gyri from the right hemisphere were also processed (dataset 2). For snRNA-seq, nuclei were loaded in the 10x Genomics chips aiming to recover 2,000–10,000 nuclei. cDNA amplification and library construction were done following 10x Genomics protocols. For both dataset 1 and dataset 2, libraries were generated using Chromium v3.1, quantified in BioAnalyzer and sequenced on an Illumina HiSeq or NovaSeq. Samples were sequenced to a depth of 40–70,000 reads per cell.

RNA *in situ* hybridization

For validation of cluster markers, mice were anesthetized and the brains were removed and placed into the ice-cold dissection solution (described above). Hippocampi were dissected under a microscope and immediately embedded in OCT on dry ice and stored at –80 °C. Sections of 14 µm covering the anterior–posterior axis of the dentate gyrus were collected in a cryostat. Sections were placed for 1 h at -20 °C and stored at –80 °C until use. Fluorescent multiplex RNA in situ hybridization was performed using the RNAscope Fluorescent Multiplex Reagent Kit (Advanced Cell Diagnostics), according to the manufacturer's instructions. Briefly, thawed sections were fixed in PFA 4%, dehydrated in sequential incubations with ethanol, followed by 30 min protease IV treatment. Mice were exposed to the enriched environment for 48h (**Figure 5E**) prior to tissue sample preparation as described above. Appropriate hybridization probes (Advanced Cell Diagnostics, catalogue#: Adamts18 452251-C1, Acvr1c 429291-C1, Nell1 807961-C2, Robo1 475951-C1, Sema3c 441441-C1) were incubated for 2 h at 40 °C, followed by amplification steps (according to protocol), DAPI counterstaining, and tissue was mounted with gerbatol to prevent bleaching.

Production of viral vectors

A replication-deficient retroviral vector based on the Moloney murine leukemia virus was used to specifically transduce aGCs as done previously [18,45]. Retroviral particles were assembled using three separate plasmids containing the capside (CMV-vsvg), viral proteins (CMV-gag/pol) and the transgenes: CAG-GFP, CAG-EGFP-IRES-Sox11 and CAG-EGFP-IRES-Sox4. Plasmids were transfected onto HEK 293T cells using deacylated polyethylenimine. HEK 293T cells were cultured in Dulbecco´s Modified Eagle´s Medium with high glucose, supplemented with 10 % fetal calf serum and 2 mM glutamine. Virus-containing supernatant was harvested 48 h after transfection and concentrated by two rounds of ultracentrifugation. Virus titer was typically ~10^5 particles/µl.

Stereotaxic surgery for retroviral delivery

Running wheel housing was only available 2-3 days before surgery to maximize the number of retrovirally transduced neurons. The wheel was removed one day after surgery. For the stereotaxic procedure, mice were anesthetized and retroviral particles were infused into the dorsal region of the right dentate gyrus (1-1.5 µl at 0.15 µl/min) using sterile calibrated microcapillary pipettes through stereotaxic references. Coordinates from bregma (mm): -2 anteroposterior, -1.5 lateral, -1.9 ventral. A single injection site was sufficient to label an abundant number of neural precursor cells. Brain sections were prepared 5 weeks post infection for immunofluorescence or electrophysiological recordings.

Immunofluorescence

Immunostaining was performed in 60 µm-thick free-floating coronal sections throughout the septal fraction of the hippocampus from *Ascl1*^{CreERT2};*CAG*$^{floxStop\text{-}Sun1/sfGFP}$ or retrovirally injected mice. Antibodies were applied in TBS with 3% donkey serum and 0.25% Triton X-100. Immunofluorescence was performed using the following primary antibodies: DCX (rabbit polyclonal; 1:1500; Abcam), GFP (chicken IgY Fraction; 1:500; Aves Labs Inc.). The following corresponding secondary antibodies were used: donkey anti-chicken Cy2 or Cy3 and donkey anti-rabbit Cy5 1:250 (Jackson ImmunoResearch Laboratories). Incubation with DAPI (10 minutes) for nuclear counterstain was performed. Slices were mounted and covered with gerbatol to prevent bleaching.

Confocal Microscopy

Sections from the septal hippocampus according to the mouse brain atlas (antero-posterior, −0.94 to −2.46 mm from bregma) were included [68]. Images were acquired using a 880 LSM Airyscan microscope (Carl Zeiss, Jena, Germany). Analysis of antibody expression was restricted to cells with fluorescence intensity levels that enabled clear identification of their soma. For Sox/GFP experiments, images were acquired (40x; NA 1.2) from 60-µm-thick sections, and colocalization was assessed using single optical planes (airy unit=1). For RNAscope experiments, images were acquired from 14 um-thick hippocampal slices. Dot area quantification was performed in ImageJ/Fiji applying the Otsu threshold as suggested by the manufacturer

(Advanced cell diagnostics). All experiments were done with control vs. treatment conditions blind to the operator.

Electrophysiology

Five weeks post retroviral injection, mice were anesthetized and brains were removed into a chilled solution containing (mM): 110 choline-Cl^-, 2.5 KCl, 2.0 NaH_2PO_4, 25 $NaHCO_3$, 0.5 $CaCl_2$, 7 $MgCl_2$, 20 dextrose, 1.3 Na^+-ascorbate, 0.6 Na^+-pyruvate, and 4 kynurenic acid. Slices (400-μm thick) were cut in a vibratome (Leica VT1200S) and transferred into a chamber containing artificial cerebrospinal fluid (ACSF; in mM): 125 NaCl, 2.5 KCl, 2.3 NaH_2PO_4, 25 $NaHCO_3$, 2 $CaCl_2$, 1.3 $MgCl_2$, 1.3 Na^+-ascorbate, 3.1 Na^+-pyruvate, and 10 dextrose (315 mOsm). Slices were maintained with 95% O_2/5% CO_2 at 30°C for >1 h before experiments started. Whole-cell recordings were performed at 23 ± 2°C using microelectrodes (3–5MΩ) pulled from borosilicate glass (KG-33; King Precision Glass) and filled with (mM): 120 K-gluconate, 20 KCl, 5 NaCl, 4 $MgCl_2$, 0.1 EGTA, 10 HEPES, 4 Tris-ATP, 0.3 Tris-GTP, 10 phosphocreatine, Alexa Fluor 488 or 594 (10 μg/ml; Invitrogen), pH 7.3, and 290 mOsm. Recordings were obtained using an Axopatch 200B amplifier (Molecular Devices), digitized (Digidata 1322A), and acquired at 10 kHz into a personal computer using the pClamp 9 software (Molecular Devices). Recorded neurons were visually identified in the granule cell layer by fluorescence (FITC fluorescence optics; DMLFS, Leica) and infrared DIC videomicroscopy. Input resistance was obtained from current traces evoked by a hyperpolarizing step of 10 mV. In current-clamp recordings the resting membrane potential was kept at -70 mV by passing a holding current. Criteria to include cells in the analysis was visual confirmation of GFP in the pipette tip, and absolute leak current <50 pA at -60 mV. Series resistance was typically <25 MΩ, and experiments were discarded if >45 MΩ. In all experiments, control or Sox11 overexpression treatments were blind to the operator.

snRNAseq processing

We used STARsolo 2.7 to align the snRNA-seq reads to the GRCm38 mouse genome. Multi-mapped reads were excluded and both exonic and intronic counts were considered. We used default parameters to count UMI and filter high-quality cells in order to generate gene-by-cell count matrices. Quality control (QC) and downstream data processing were performed using *scran* and *scDblFinder* bioconductor libraries [69,70]. All scripts used to perform the present analysis were included in the companion website https://github.com/chernolabs/NeuronalSwitch.

For dataset 1, we removed 80 nuclei with <1000 detected features, and 636 nuclei identified as doublets by scDblFinder out of the 17046 nuclei that passed the STARsolo quality filter. We also eliminated 839 low-quality nuclei identified either by: 1) a multivariate outlier detection procedure (adjOutlyingness function of robustbase R library) based on low library sizes, low number of detected features and large mitochondrial (Mt) content, or 2) presenting more than 1% of Mt counts. Features with >20 molecules and detected in >1% and <80% of filtered nuclei were retained. In addition, we removed specific genes (*Ehd2, Espl1, Jarid1d,*

Pnpla4, Rps4y1, Xist, Tsix, Eif2s3y, Ddx3y, Uty, Kdm5d, Rpl26, Gstp1, Rpl35a, Erh, Slc25a5, Pgk1, Eno1, Tubb2a, Emc4, Scg5) to mitigate possible sex and stress effects on downstream analysis [28]. The data was normalized using the scran library in accordance with the OSCA pipeline [71]. We executed a quick clustering for each timepoint independently, normalized nuclei in each cluster separately, and rescaled the size factors to be comparable across clusters. Finally, we computed the log2 of the data and considered a pseudo-count value of 1 to generate a normalized expression matrix. After scaling and log-normalizing gene expression values, we used the scran *modelGeneVar* function to identify the 3000 most variable genes in their log-expression profiles.

For dataset 2, 32,621 nuclei successfully passed the STARsolo quality filter. Subsequently, we identified and discarded 1,015 doublets and 4,808 low-quality nuclei using the QC protocol applied to dataset 1. The entire curation process yielded a high-quality dataset comprising 26,798 nuclei and 14,220 informative features. We considered inter-nuclei similarities using the Pearson correlation measure within the subspace spanned by the top 20 principal components. We finally retained for further analysis 26,716 nuclei that were part of graph components larger than 30 nodes. We then used the *batchelor* Bioconductor package to investigate the biological reproducibility between datasets 1 and 2. Some dataset 1 nuclei occupied a region in reduced-dimensionality spaces (PCA, t-SNE, UMAP) not represented in dataset 2. Employing a k=20 mKNN-graph estimated from the largest 20 PCA components (similarities obtained from Pearson correlation values), we verified that these nuclei formed two Louvain clusters composed of 1071 nuclei from 4-week-old samples. Noticeably, we found that 85% of nuclei in these clusters exhibited higher expression of male-associated genes (*Ddx3y*, *Uty*, *Eif2s3y*) than female-associated genes (*Xist*, *Tsix*), suggesting that they could belong to a single male mouse, potentially a biological outlier. Therefore, we re-processed *de-novo* dataset 1, excluding these nuclei which resulted in 14,441 high-quality nuclei and 13,353 features. To get a proxy of the biologically relevant manifold, we constructed a mKNN graph (k=40) considering the Pearson correlation similarity measure estimated from the 20 largest PCA components. As we did with dataset 2, we discarded nuclei that were found in small components (<30 elements) of this mKNN graph. The remaining 14,367 nuclei were grouped into communities considering the Louvain algorithm. This initial graph-based clustering was further refined to produce 13 communities for which specific markers were identified (see Results section). We determined differentially expressed genes between nuclei groups using the *FindMarkers* function from the *scran* library (*t*-test pairwise). Cluster marker genes were identified as highly ranked differentially expressed genes between the query group and all other clusters.

TF expression cascades

We considered 703 mouse TFs listed in the *dorothea* 1.8.0 R package that passed the quality control feature filtering step [72]. We tested whether these genes were significantly expressed along the pseudotime coordinate using the *difftest* function of the TSCAN 1.34 R package. Likelihood ratio tests were performed to compare a generalized additive model with a constant fit to get the p-values, with 201 TFs showing FDR

adjusted q-value <0.05. A custom script was used to identify TFs that were shutdown (80) or turned on (43) at specific clusters in this dataset (**Figure 6A,B**).

Gene Ontology analysis

GO enrichment analyses was performed using ShinyGO 0.77 (http://bioinformatics.sdstate.edu/go/) [73].

Pseudotime determination

The *slingshot* 2.4.0 R-package was used to fit developmental trajectories to nuclei of the following clusters: RGL, NPC, NB1, NB2, GCimm1, GCimm2, GCyoung and GCmat1 [74]. We excluded from this analysis GCmat2 nuclei and 383 GCmat1 nuclei with strong expression signal of ventral genes (**see FigS7C**). We considered the UMAP (3D) low dimensional coordinates to fit principal curves and produce pseudotime estimations (PCA-3dim and PCA-20dim produced similar density profiles along the corresponding pseudotime coordinates). A similar procedure was used for dataset 2.

SCENIC regulons

To analyze the transcriptional changes occurring when neurons become mature, we considered 3-, 4-, 5-, and 8-week cohorts of dataset 2 and selected nuclei located around the 3rd and 4th peak of the pseudotime density distribution (19.4±2.5 and 30.3±2.5 pseudotime intervals in **Figure 6C**), containing 4855 and 4244 nuclei respectively. We used the *SCENIC* 1.3.1 R-package to analyze the expression of relevant TFs and their targets (regulons) [75]. We used the calcRSS function to estimate Regulon Specificity Scores [76]**.**

Visualization and graphical reports

We used Force Atlas 2 layout algorithm, implemented in Gephi to produce 2-dim visualization of mKNN graphs [77]. Heatmaps, volcano plots, violin plots, dot plots, and spike plots were produced using the scX R package [https://chernolabs.github.io/scX/].

REFERENCES

1. Hainmueller, T., and Bartos, M. (2020). Dentate gyrus circuits for encoding, retrieval and discrimination of episodic memories. Nature reviews. Neuroscience *21*, 153-168. 10.1038/s41583-019-0260-z.
2. Johnston, D., and Amaral, D.G. (2004). Hippocampus. In The Synaptic Organization of the Brain, G.M. Shepherd, ed. (Oxford University Press), pp. 0. 10.1093/acprof:oso/9780195159561.003.0011.
3. Schinder, A.F., Trinchero, M.F., and Groisman, A.I. (2020). Chapter 10 - Synaptogenesis in the adult CNS—Hippocampus. In Synapse Development and Maturation, J. Rubenstein, P. Rakic, B. Chen, K.Y.

Kwan, H.T. Cline, and J. Cardin, eds. (Academic Press), pp. 235-253. https://doi.org/10.1016/B978-0-12-823672-7.00010-7.

4. Goncalves, J.T., Schafer, S.T., and Gage, F.H. (2016). Adult Neurogenesis in the Hippocampus: From Stem Cells to Behavior. Cell *167*, 897-914. 10.1016/j.cell.2016.10.021.
5. Olpe, C., and Jessberger, S. (2023). Cell population dynamics in the course of adult hippocampal neurogenesis: Remaining unknowns. Hippocampus *33*, 402-411. 10.1002/hipo.23475.
6. Drew, L.J., Fusi, S., and Hen, R. (2013). Adult neurogenesis in the mammalian hippocampus: why the dentate gyrus? Learning & memory *20*, 710-729. 10.1101/lm.026542.112.
7. Kropff, E., Yang, S.M., and Schinder, A.F. (2015). Dynamic role of adult-born dentate granule cells in memory processing. Current opinion in neurobiology *35*, 21-26. 10.1016/j.conb.2015.06.002.
8. Piatti, V.C., Ewell, L.A., and Leutgeb, J.K. (2013). Neurogenesis in the dentate gyrus: carrying the message or dictating the tone. Frontiers in neuroscience *7*, 50. 10.3389/fnins.2013.00050.
9. Adlaf, E.W., Vaden, R.J., Niver, A.J., Manuel, A.F., Onyilo, V.C., Araujo, M.T., Dieni, C.V., Vo, H.T., King, G.D., Wadiche, J.I., and Overstreet-Wadiche, L. (2017). Adult-born neurons modify excitatory synaptic transmission to existing neurons. eLife *6*. 10.7554/eLife.19886.
10. Sailor, K.A., Schinder, A.F., and Lledo, P.M. (2017). Adult neurogenesis beyond the niche: its potential for driving brain plasticity. Current opinion in neurobiology *42*, 111-117. 10.1016/j.conb.2016.12.001.
11. Toni, N., Laplagne, D.A., Zhao, C., Lombardi, G., Ribak, C.E., Gage, F.H., and Schinder, A.F. (2008). Neurons born in the adult dentate gyrus form functional synapses with target cells. Nature neuroscience *11*, 901-907. 10.1038/nn.2156.
12. Toni, N., Teng, E.M., Bushong, E.A., Aimone, J.B., Zhao, C., Consiglio, A., van Praag, H., Martone, M.E., Ellisman, M.H., and Gage, F.H. (2007). Synapse formation on neurons born in the adult hippocampus. Nature neuroscience *10*, 727-734. 10.1038/nn1908.
13. Kohler, S.J., Williams, N.I., Stanton, G.B., Cameron, J.L., and Greenough, W.T. (2011). Maturation time of new granule cells in the dentate gyrus of adult macaque monkeys exceeds six months. Proceedings of the National Academy of Sciences of the United States of America *108*, 10326-10331. 10.1073/pnas.1017099108.
14. Bergami, M., Masserdotti, G., Temprana, S.G., Motori, E., Eriksson, T.M., Gobel, J., Yang, S.M., Conzelmann, K.K., Schinder, A.F., Gotz, M., and Berninger, B. (2015). A critical period for experience-dependent remodeling of adult-born neuron connectivity. Neuron *85*, 710-717. 10.1016/j.neuron.2015.01.001.
15. Ge, S., Yang, C.H., Hsu, K.S., Ming, G.L., and Song, H. (2007). A critical period for enhanced synaptic plasticity in newly generated neurons of the adult brain. Neuron *54*, 559-566. 10.1016/j.neuron.2007.05.002.

16. Gu, Y., Arruda-Carvalho, M., Wang, J., Janoschka, S.R., Josselyn, S.A., Frankland, P.W., and Ge, S. (2012). Optical controlling reveals time-dependent roles for adult-born dentate granule cells. Nature neuroscience *15*, 1700-1706. 10.1038/nn.3260.

17. Jungenitz, T., Beining, M., Radic, T., Deller, T., Cuntz, H., Jedlicka, P., and Schwarzacher, S.W. (2018). Structural homo- and heterosynaptic plasticity in mature and adult newborn rat hippocampal granule cells. Proceedings of the National Academy of Sciences of the United States of America *115*, E4670-E4679. 10.1073/pnas.1801889115.

18. Marin-Burgin, A., Mongiat, L.A., Pardi, M.B., and Schinder, A.F. (2012). Unique processing during a period of high excitation/inhibition balance in adult-born neurons. Science *335*, 1238-1242. 10.1126/science.1214956.

19. McHugh, S.B., Lopes-Dos-Santos, V., Gava, G.P., Hartwich, K., Tam, S.K.E., Bannerman, D.M., and Dupret, D. (2022). Adult-born dentate granule cells promote hippocampal population sparsity. Nature neuroscience *25*, 1481-1491. 10.1038/s41593-022-01176-5.

20. Mugnaini, M., Trinchero, M.F., Schinder, A.F., Piatti, V.C., and Kropff, E. (2023). Unique potential of immature adult-born neurons for the remodeling of CA3 spatial maps. Cell reports *42*, 113086. 10.1016/j.celrep.2023.113086.

21. Restivo, L., Niibori, Y., Mercaldo, V., Josselyn, S.A., and Frankland, P.W. (2015). Development of Adult-Generated Cell Connectivity with Excitatory and Inhibitory Cell Populations in the Hippocampus. The Journal of neuroscience : the official journal of the Society for Neuroscience *35*, 10600-10612. 10.1523/JNEUROSCI.3238-14.2015.

22. Schmidt-Hieber, C., Jonas, P., and Bischofberger, J. (2004). Enhanced synaptic plasticity in newly generated granule cells of the adult hippocampus. Nature *429*, 184-187. 10.1038/nature02553.

23. Laplagne, D.A., Esposito, M.S., Piatti, V.C., Morgenstern, N.A., Zhao, C., van Praag, H., Gage, F.H., and Schinder, A.F. (2006). Functional convergence of neurons generated in the developing and adult hippocampus. PLoS biology *4*, e409. 10.1371/journal.pbio.0040409.

24. Laplagne, D.A., Kamienkowski, J.E., Esposito, M.S., Piatti, V.C., Zhao, C., Gage, F.H., and Schinder, A.F. (2007). Similar GABAergic inputs in dentate granule cells born during embryonic and adult neurogenesis. The European journal of neuroscience *25*, 2973-2981. 10.1111/j.1460-9568.2007.05549.x.

25. Bottes, S., Jaeger, B.N., Pilz, G.A., Jorg, D.J., Cole, J.D., Kruse, M., Harris, L., Korobeynyk, V.I., Mallona, I., Helmchen, F., et al. (2021). Long-term self-renewing stem cells in the adult mouse hippocampus identified by intravital imaging. Nature neuroscience *24*, 225-233. 10.1038/s41593-020-00759-4.

26. Shin, J., Berg, D.A., Zhu, Y., Shin, J.Y., Song, J., Bonaguidi, M.A., Enikolopov, G., Nauen, D.W., Christian, K.M., Ming, G.L., and Song, H. (2015). Single-Cell RNA-Seq with Waterfall Reveals Molecular Cascades underlying Adult Neurogenesis. Cell stem cell *17*, 360-372. 10.1016/j.stem.2015.07.013.

27. Habib, N., Li, Y., Heidenreich, M., Swiech, L., Avraham-Davidi, I., Trombetta, J.J., Hession, C., Zhang, F., and Regev, A. (2016). Div-Seq: Single-nucleus RNA-Seq reveals dynamics of rare adult newborn neurons. Science *353*, 925-928. 10.1126/science.aad7038.

28. Hochgerner, H., Zeisel, A., Lonnerberg, P., and Linnarsson, S. (2018). Conserved properties of dentate gyrus neurogenesis across postnatal development revealed by single-cell RNA sequencing. Nature neuroscience *21*, 290-299. 10.1038/s41593-017-0056-2.

29. Kim, E.J., Leung, C.T., Reed, R.R., and Johnson, J.E. (2007). In vivo analysis of Ascl1 defined progenitors reveals distinct developmental dynamics during adult neurogenesis and gliogenesis. The Journal of neuroscience : the official journal of the Society for Neuroscience *27*, 12764-12774. 10.1523/JNEUROSCI.3178-07.2007.

30. Yang, S.M., Alvarez, D.D., and Schinder, A.F. (2015). Reliable Genetic Labeling of Adult-Born Dentate Granule Cells Using Ascl1 CreERT2 and Glast CreERT2 Murine Lines. The Journal of neuroscience : the official journal of the Society for Neuroscience *35*, 15379-15390. 10.1523/JNEUROSCI.2345-15.2015.

31. Mo, A., Mukamel, E.A., Davis, F.P., Luo, C., Henry, G.L., Picard, S., Urich, M.A., Nery, J.R., Sejnowski, T.J., Lister, R., et al. (2015). Epigenomic Signatures of Neuronal Diversity in the Mammalian Brain. Neuron *86*, 1369-1384. 10.1016/j.neuron.2015.05.018.

32. Blondel, V.D., Guillaume, J.-L., Lambiotte, R., and Lefebvre, E. (2008). Fast unfolding of communities in large networks. Journal of Statistical Mechanics: Theory and Experiment *P10008*, 1-12. 10.1088/1742-5468/2008/10/p10008.

33. Gebara, E., Bonaguidi, M.A., Beckervordersandforth, R., Sultan, S., Udry, F., Gijs, P.J., Lie, D.C., Ming, G.L., Song, H., and Toni, N. (2016). Heterogeneity of Radial Glia-Like Cells in the Adult Hippocampus. Stem cells *34*, 997-1010. 10.1002/stem.2266.

34. Esposito, M.S., Piatti, V.C., Laplagne, D.A., Morgenstern, N.A., Ferrari, C.C., Pitossi, F.J., and Schinder, A.F. (2005). Neuronal differentiation in the adult hippocampus recapitulates embryonic development. The Journal of neuroscience : the official journal of the Society for Neuroscience *25*, 10074-10086. 10.1523/JNEUROSCI.3114-05.2005.

35. Mathews, E.A., Morgenstern, N.A., Piatti, V.C., Zhao, C., Jessberger, S., Schinder, A.F., and Gage, F.H. (2010). A distinctive layering pattern of mouse dentate granule cells is generated by developmental and adult neurogenesis. The Journal of comparative neurology *518*, 4479-4490. 10.1002/cne.22489.

36. Yasuda, R., Hayashi, Y., and Hell, J.W. (2022). CaMKII: a central molecular organizer of synaptic plasticity, learning and memory. Nature reviews. Neuroscience *23*, 666-682. 10.1038/s41583-022-00624-2.

37. Chater, T.E., and Goda, Y. (2022). The Shaping of AMPA Receptor Surface Distribution by Neuronal Activity. Frontiers in synaptic neuroscience *14*, 833782. 10.3389/fnsyn.2022.833782.

38. Gambrill, A.C., and Barria, A. (2011). NMDA receptor subunit composition controls synaptogenesis and synapse stabilization. Proceedings of the National Academy of Sciences of the United States of America *108*, 5855-5860. 10.1073/pnas.1012676108.

39. Cembrowski, M.S., Wang, L., Sugino, K., Shields, B.C., and Spruston, N. (2016). Hipposeq: a comprehensive RNA-seq database of gene expression in hippocampal principal neurons. eLife *5*, e14997. 10.7554/eLife.14997.

40. Fanselow, M.S., and Dong, H.W. (2010). Are the dorsal and ventral hippocampus functionally distinct structures? Neuron *65*, 7-19. 10.1016/j.neuron.2009.11.031.

41. Jaeger, B.N., Linker, S.B., Parylak, S.L., Barron, J.J., Gallina, I.S., Saavedra, C.D., Fitzpatrick, C., Lim, C.K., Schafer, S.T., Lacar, B., et al. (2018). A novel environment-evoked transcriptional signature predicts reactivity in single dentate granule neurons. Nature communications *9*, 3084. 10.1038/s41467-018-05418-8.

42. De Vincenti, A.P., Rios, A.S., Paratcha, G., and Ledda, F. (2019). Mechanisms That Modulate and Diversify BDNF Functions: Implications for Hippocampal Synaptic Plasticity. Frontiers in cellular neuroscience *13*, 135. 10.3389/fncel.2019.00135.

43. Park, H., and Poo, M.M. (2013). Neurotrophin regulation of neural circuit development and function. Nature reviews. Neuroscience *14*, 7-23. 10.1038/nrn3379.

44. Gao, Y., Shen, M., Gonzalez, J.C., Dong, Q., Kannan, S., Hoang, J.T., Eisinger, B.E., Pandey, J., Javadi, S., Chang, Q., et al. (2020). RGS6 Mediates Effects of Voluntary Running on Adult Hippocampal Neurogenesis. Cell reports *32*, 107997. 10.1016/j.celrep.2020.107997.

45. Alvarez, D.D., Giacomini, D., Yang, S.M., Trinchero, M.F., Temprana, S.G., Buttner, K.A., Beltramone, N., and Schinder, A.F. (2016). A disynaptic feedback network activated by experience promotes the integration of new granule cells. Science *354*, 459-465. 10.1126/science.aaf2156.

46. Hillary, R.F., and FitzGerald, U. (2018). A lifetime of stress: ATF6 in development and homeostasis. Journal of biomedical science *25*, 48. 10.1186/s12929-018-0453-1.

47. Schaffner, I., Minakaki, G., Khan, M.A., Balta, E.A., Schlotzer-Schrehardt, U., Schwarz, T.J., Beckervordersandforth, R., Winner, B., Webb, A.E., DePinho, R.A., et al. (2018). FoxO Function Is Essential for Maintenance of Autophagic Flux and Neuronal Morphogenesis in Adult Neurogenesis. Neuron *99*, 1188-1203 e1186. 10.1016/j.neuron.2018.08.017.

48. Scobie, K.N., Hall, B.J., Wilke, S.A., Klemenhagen, K.C., Fujii-Kuriyama, Y., Ghosh, A., Hen, R., and Sahay, A. (2009). Kruppel-like factor 9 is necessary for late-phase neuronal maturation in the developing dentate gyrus and during adult hippocampal neurogenesis. The Journal of neuroscience : the official journal of the Society for Neuroscience *29*, 9875-9887. 10.1523/JNEUROSCI.2260-09.2009.

49. Valakh, V., Wise, D., Zhu, X.A., Sha, M., Fok, J., Van Hooser, S.D., Schectman, R., Cepeda, I., Kirk, R., O'Toole, S.M., and Nelson, S.B. (2023). A transcriptional constraint mechanism limits the homeostatic response to activity deprivation in mammalian neocortex. eLife *12*. 10.7554/eLife.74899.

50. Calderari, S., Ria, M., Gerard, C., Nogueira, T.C., Villate, O., Collins, S.C., Neil, H., Gervasi, N., Hue, C., Suarez-Zamorano, N., et al. (2018). Molecular genetics of the transcription factor GLIS3 identifies its dual function in beta cells and neurons. Genomics *110*, 98-111. 10.1016/j.ygeno.2017.09.001.

51. Haslinger, A., Schwarz, T.J., Covic, M., and Lie, D.C. (2009). Expression of Sox11 in adult neurogenic niches suggests a stage-specific role in adult neurogenesis. The European journal of neuroscience *29*, 2103-2114. 10.1111/j.1460-9568.2009.06768.x.

52. Mu, L., Berti, L., Masserdotti, G., Covic, M., Michaelidis, T.M., Doberauer, K., Merz, K., Rehfeld, F., Haslinger, A., Wegner, M., et al. (2012). SoxC transcription factors are required for neuronal differentiation in adult hippocampal neurogenesis. The Journal of neuroscience : the official journal of the Society for Neuroscience *32*, 3067-3080. 10.1523/JNEUROSCI.4679-11.2012.

53. Mongiat, L.A., Esposito, M.S., Lombardi, G., and Schinder, A.F. (2009). Reliable activation of immature neurons in the adult hippocampus. PloS one *4*, e5320. 10.1371/journal.pone.0005320.

54. Piatti, V.C., Davies-Sala, M.G., Esposito, M.S., Mongiat, L.A., Trinchero, M.F., and Schinder, A.F. (2011). The timing for neuronal maturation in the adult hippocampus is modulated by local network activity. The Journal of neuroscience : the official journal of the Society for Neuroscience *31*, 7715-7728. 10.1523/JNEUROSCI.1380-11.2011.

55. Kalinina, A., and Lagace, D. (2022). Single-Cell and Single-Nucleus RNAseq Analysis of Adult Neurogenesis. Cells *11*. 10.3390/cells11101633.

56. Hodge, R.D., Kowalczyk, T.D., Wolf, S.A., Encinas, J.M., Rippey, C., Enikolopov, G., Kempermann, G., and Hevner, R.F. (2008). Intermediate progenitors in adult hippocampal neurogenesis: Tbr2 expression and coordinate regulation of neuronal output. The Journal of neuroscience : the official journal of the Society for Neuroscience *28*, 3707-3717. 10.1523/JNEUROSCI.4280-07.2008.

57. Steiner, B., Klempin, F., Wang, L., Kott, M., Kettenmann, H., and Kempermann, G. (2006). Type-2 cells as link between glial and neuronal lineage in adult hippocampal neurogenesis. Glia *54*, 805-814. 10.1002/glia.20407.

58. Chancey, J.H., Adlaf, E.W., Sapp, M.C., Pugh, P.C., Wadiche, J.I., and Overstreet-Wadiche, L.S. (2013). GABA depolarization is required for experience-dependent synapse unsilencing in adult-born neurons. The Journal of neuroscience : the official journal of the Society for Neuroscience *33*, 6614-6622. 10.1523/JNEUROSCI.0781-13.2013.

59. Ge, S., Goh, E.L., Sailor, K.A., Kitabatake, Y., Ming, G.L., and Song, H. (2006). GABA regulates synaptic integration of newly generated neurons in the adult brain. Nature *439*, 589-593. 10.1038/nature04404.

60. Zhao, C., Teng, E.M., Summers, R.G., Jr., Ming, G.L., and Gage, F.H. (2006). Distinct morphological stages of dentate granule neuron maturation in the adult mouse hippocampus. The Journal of neuroscience : the official journal of the Society for Neuroscience *26*, 3-11. 10.1523/JNEUROSCI.3648-05.2006.

61. Groisman, A.I., Yang, S.M., and Schinder, A.F. (2020). Differential Coupling of Adult-Born Granule Cells to Parvalbumin and Somatostatin Interneurons. Cell reports *30*, 202-214 e204. 10.1016/j.celrep.2019.12.005.

62. Dieni, C.V., Panichi, R., Aimone, J.B., Kuo, C.T., Wadiche, J.I., and Overstreet-Wadiche, L. (2016). Low excitatory innervation balances high intrinsic excitability of immature dentate neurons. Nature communications *7*, 11313. 10.1038/ncomms11313.

63. Naranjo, J.R., Zhang, H., Villar, D., Gonzalez, P., Dopazo, X.M., Moron-Oset, J., Higueras, E., Oliveros, J.C., Arrabal, M.D., Prieto, A., et al. (2016). Activating transcription factor 6 derepression mediates neuroprotection in Huntington disease. The Journal of clinical investigation *126*, 627-638. 10.1172/JCI82670.

64. Nakao, A., Miyazaki, N., Ohira, K., Hagihara, H., Takagi, T., Usuda, N., Ishii, S., Murata, K., and Miyakawa, T. (2017). Immature morphological properties in subcellular-scale structures in the dentate gyrus of Schnurri-2 knockout mice: a model for schizophrenia and intellectual disability. Molecular brain *10*, 60. 10.1186/s13041-017-0339-2.

65. Kim, E.J., Ables, J.L., Dickel, L.K., Eisch, A.J., and Johnson, J.E. (2011). Ascl1 (Mash1) defines cells with long-term neurogenic potential in subgranular and subventricular zones in adult mouse brain. PloS one *6*, e18472. 10.1371/journal.pone.0018472.

66. Hagihara, H., Toyama, K., Yamasaki, N., and Miyakawa, T. (2009). Dissection of hippocampal dentate gyrus from adult mouse. Journal of visualized experiments : JoVE. 10.3791/1543.

67. Habib, N., Avraham-Davidi, I., Basu, A., Burks, T., Shekhar, K., Hofree, M., Choudhury, S.R., Aguet, F., Gelfand, E., Ardlie, K., et al. (2017). Massively parallel single-nucleus RNA-seq with DroNc-seq. Nature methods *14*, 955-958. 10.1038/nmeth.4407.

68. Paxinos, G., and Franklin, K.B.J. (2001). The Mouse Brain in Stereotaxic Coordinates (Academic Press).

69. Germain, P.L., Lun, A., Garcia Meixide, C., Macnair, W., and Robinson, M.D. (2021). Doublet identification in single-cell sequencing data using scDblFinder. F1000Research *10*, 979. 10.12688/f1000research.73600.2.

70. Lun, A.T., McCarthy, D.J., and Marioni, J.C. (2016). A step-by-step workflow for low-level analysis of single-cell RNA-seq data with Bioconductor. F1000Research *5*, 2122. 10.12688/f1000research.9501.2.

71. Amezquita, R.A., Lun, A.T.L., Becht, E., Carey, V.J., Carpp, L.N., Geistlinger, L., Marini, F., Rue-Albrecht, K., Risso, D., Soneson, C., et al. (2020). Orchestrating single-cell analysis with Bioconductor. Nature methods *17*, 137-145. 10.1038/s41592-019-0654-x.

72. Holland, C.H., Szalai, B., and Saez-Rodriguez, J. (2020). Transfer of regulatory knowledge from human to mouse for functional genomics analysis. Biochimica et biophysica acta. Gene regulatory mechanisms *1863*, 194431. 10.1016/j.bbagrm.2019.194431.

73. Ge, S.X., Jung, D., and Yao, R. (2020). ShinyGO: a graphical gene-set enrichment tool for animals and plants. Bioinformatics *36*, 2628-2629. 10.1093/bioinformatics/btz931.

74. Street, K., Risso, D., Fletcher, R.B., Das, D., Ngai, J., Yosef, N., Purdom, E., and Dudoit, S. (2018). Slingshot: cell lineage and pseudotime inference for single-cell transcriptomics. BMC genomics *19*, 477. 10.1186/s12864-018-4772-0.

75. Aibar, S., Gonzalez-Blas, C.B., Moerman, T., Huynh-Thu, V.A., Imrichova, H., Hulselmans, G., Rambow, F., Marine, J.C., Geurts, P., Aerts, J., et al. (2017). SCENIC: single-cell regulatory network inference and clustering. Nature methods *14*, 1083-1086. 10.1038/nmeth.4463.

76. Suo, S., Zhu, Q., Saadatpour, A., Fei, L., Guo, G., and Yuan, G.C. (2018). Revealing the Critical Regulators of Cell Identity in the Mouse Cell Atlas. Cell reports *25*, 1436-1445 e1433. 10.1016/j.celrep.2018.10.045.

77. Bastian, M., Heymann, S., and Jacomy, M. (2009). Gephi: An Open Source Software for Exploring and Manipulating Networks. Proceedings of the International AAAI Conference on Web and Social Media *3*, 361-362. 10.1609/icwsm.v3i1.13937.

78. Trinchero, M.F., Giacomini, D., and Schinder, A.F. (2021). Dynamic interplay between GABAergic networks and developing neurons in the adult hippocampus. Current opinion in neurobiology *69*, 124-130. 10.1016/j.conb.2021.03.008.

FIGURE LEGENDS

Figure 1. Transcriptional dynamics of neuronal cohorts born in the adult dentate gyrus. (A) Schematic representation of developing aGCs in the adult hippocampus. RGLs have the potential to give rise to both astrocytes and neurons. Adult neurogenesis can be divided in 4 phases. Phase I: RGLs divide and differentiate to NPCs, which subsequently give rise to NBs. New aGCs receive dendritic depolarizing GABAergic inputs. Phase II: developing aGCs acquire glutamatergic contacts. Phase III: period of enhanced excitation/inhibition balance and high excitability. Phase IV: all inputs including perisomatic GABAergic inhibition become mature and excitability decreases [78]. Colored bars denote the expression of GFAP (astrocytic lineage), DCX and Calb1 (neuronal lineage). **(B)** Experimental design. *Ascl1*^{CreERT2}*;CAG* $^{floxStop\text{-}Sun1/sfGFP}$ mice received tamoxifen (TAM) injections to label nuclei from the progeny of RGLs and NPCs. Dentate gyri were microdissected at indicated time points. The confocal image below depicts a dentate gyrus with Sun1/sfGFP-labeled nuclei from 2-week-old aGCs. Scale bar: 100 µm. **(C)** T-distributed stochastic neighbor embedding (t-SNE) visualizations for individual neuronal cohorts collected at 1, 2, 4 and 8 weeks after labeling (total: 14,367 nuclei). **(D)** Mutual *k* nearest neighbor (mKNN, *k*=40) graph displaying 13 clusters indicated by color and number. The red arrow denotes the path followed by the process of adult neurogenesis from the least- to the most advanced stages. **(E)** Heatmap showing the normalized expression for 100 genes with highest variability (listed in **Table S1**), which highlights the specific transcriptomic signature for each cluster. Numbers and colors correspond to clusters shown in (D). Maximal expression of each gene is shown on the left (Max. value). Pseudocolor scale on the right denotes mean expression level. **(F)** Dot plot exhibiting canonical markers for neuronal and non-neuronal phenotypes. Pericyte (Peri): *Tbx18* and *Slc6a13*; Oligodendrocyte (Oligo): *Mag* and *Mog*; Oligodendrocyte progenitor (OPC): *Prkg2* and *Cspg4*; astrocyte (Astro): *Gfap, Slc7a10* and *Slc1a2*; RGL: *Hopx* and *Notch2*; neurons: *Dcx, Rbfox3* and *Prox1*. Scales on the right correspond to log2(mean gene expression) (color) and to the fraction of nuclei expressing at least one transcript count in the cluster (dot size). All data in the figure correspond to dataset 1.

Figure 2. Timing and complexity of adult neurogenesis revealed by molecular profiling. (A) mKNN graph displaying cluster identity based on the expression of canonical genes: RGL (radial glia-like cell), NPC (neuronal progenitor cell), NB (neuroblast), GCimm (immature aGC), GCyoung (young aGC), GCmat (mature aGC), Astro (astrocyte), OPC (oligodendrocyte progenitor cell), Oligo (oligodendrocyte) and Peri (pericyte). **(B)** Violin plots showing the expression level of canonical marker genes for the defined clusters. **(C)** Progression of each cohort and their localization over the mKNN graph. Nuclei density is indicated by the yellow (low) to red (high) gradient. **(D)** Nuclei distribution for each cohort along clusters. **(E)** Differentially expressed genes (DEGs; **Table S2**) between adjacent cluster transitions indicated above. Additional comparisons (non-adjacent) are shown on the right. Up- and downregulated genes are shown in red and blue. All data in the figure correspond to dataset 1.

Figure 3. Major switches in gene profiles and biological processes during early neuronal commitment. (A) Schematic mKNN graph depicting the analyzed transitions (red lines). **(B, C)** Analysis of RGL to NPC **(B)** and NPC to NB1 transitions **(C).** Upper panels: volcano plots showing differential expression analysis (FC ≥ 1.5 or ≤ -1.5 and FDR ≤ 0.05) displaying relevant gene examples. FC: fold change. FDR: false discovery rate. Lower panels: spike plots displaying mean expression of down- and upregulated DEGs for all nuclei ordered according to their estimated pseudotime value. Black dashes show the mean expression for each cluster and the red asterisks highlight the analyzed transitions. **(D)** Top GO biological processes for the enrichment analysis of DEGs in the transition from NPC to NB1. FDR cutoff = 0.05. **(E)** NB1 vs NB2 comparison. Upper panel: volcano plot displaying relevant gene examples. Lower panel: heatmap showing the row-wise normalized expression of up- (red) and downregulated DEGs (blue) across clusters. Pseudocolor scale on the right denotes mean expression level. All data in the figure correspond to dataset 1. All DEGs are listed in **Table S2.**

Figure 4. Upregulation of effector genes required for neuronal function in immature aGCs. (A) Schematic mKNN graph depicting the analyzed transitions (red lines). **(B, C)** Analysis of NB1 to GCimm1 **(B)** and GCimm1 to GCimm2 transitions **(C).** Upper panels: volcano plots showing differential expression analysis (FC ≥ 1.5 or ≤ -1.5 and FDR ≤ 0.05) with relevant gene examples. Lower panels: heatmap showing the row-wise normalized expression of up- (red) and downregulated DEGs (blue) across clusters (top 50 genes per transition). Pseudocolor scale on the right denotes mean expression level. **(D)** Spike plots showing the mean expression of genes relevant for neurotransmission (**Table S4**). Nuclei were ordered according to their estimated pseudotime value . Black dashes show the mean expression for each cluster. All data in the figure correspond to dataset 1.

Figure 5. Gene expression during late maturation of aGCs. (A) Schematic mKNN graph depicting the analyzed transitions (red lines). **(B)** Violin plots showing example genes critical for aGC function. **(C)** Dot plot exhibiting genes selectively up- and downregulated in GCmat1. Scales on the right correspond to mean expression levels (color) and to the fraction of nuclei expressing at least one transcript count in the cluster (dot size). **(D)** Violin plots depicting the expression of transcripts that are known to be induced by activity (Jaeger et al 2018). All data in the figure correspond to dataset 1. **(E)** *In situ* hybridization reveals the expression of the activity-induced gene *Acvr1c* in the granule cell layer. Mice were exposed to an enriched environment for 2 days (EE) or remained in a home cage (control). Left panels display representative single plane images depicting *Acvr1c* expression (red; DAPI, grey). Scale bar: 20 µm. Right panel: dentate gyrus area occupied by Acvr1c fluorescence in control and EE mice. N = 10 sections / 4 mice (control) and N = 15 sections / 4 mice (EE). (*) denotes $p<0.02$ after Mann Whitney's test. Data depicts mean±SEM.

Figure 6. A developmental trajectory defined by four cellular states. (A,B) Heatmaps displaying the row-wise normalized expression of transcription factors with sharp transitions switching OFF **(A)** or ON **(B)** across clusters. Genes are ordered by the pseudotime of their switching event. Maximum expression (MaxExp) is shown on the left (colored scale on the right). Color-coded clusters are indicated below. **(C)** Density distribution of nuclei along the pseudotime progression for each cohort in dataset 2. Pseudotime values were assigned based on their profile and organized in density plots. The data revealed four cellular states with distinct cluster composition: 1st RGL; 2nd NPC; 3rd NB1-GCimm1-Gcimm2; 4th GCyoung-GCmat1. Dashed lines depict major transitions in gene profile expression. Color codes below denote cluster identity. **(D)** Regulon activity analysis based on the expression levels of TF targets comparing the 3rd and 4th states shown in (C). Each regulon contains targets genes identified by SCENIC according to the conserved DNA binding motifs in regulatory regions. Regulon sizes are shown in parentheses. Extended regulons include targets inferred by binding motif similarity. Regulon compositions are listed in **Table S5.** RSS: Regulon specificity score [76]. The z score color scale depicts standardized expression activity values.

Figure 7. Overexpression of SoxC transcription factors precludes aGC maturation. (A) New aGCs were labeled in adult mice by stereotaxic delivery of RV-GFP, RV-Sox11-GFP or RV-Sox4-GFP, as indicated. aGCs expressing GFP were studied 5 weeks post injection. (**B,C**) Representative single confocal planes displaying aGCs expressing Sox11-GFP, Sox4-GFP or control GFP (green, arrowheads) and DCX (yellow). Colocalization is highlighted by white arrows. Scale bar: 20 μm. **(C)** Proportion of GFP$^+$ neurons expressing DCX, normalized to the total number of GFP$^+$ neurons. N = 80 aGCs from 4 mice for each condition. (*) denotes $p<0.02$, Kruskal-Wallis test. **(D-H)** Whole-cell recordings in acute slices from aGCs expressing RV-GFP or RV-Sox11-GFP. (**D**) Input resistance. GFP-aGCs N = 13; Sox11-aGCs, N = 10 (4 mice/condition). (**) denotes $p<0.005$, *t*-test. **(E)** Representative voltage traces elicited by current steps of increasing amplitude: 5, 20, 40, 60 and 95 pA. Scale: 50 mV, 100 ms. $V_{resting}$ kept at -80 mV. **(F-H)** Action potentials elicited by injected current steps (500 ms). Plots show the total number of spikes per pulse (**F**), the amplitude of the first spike **(G)**, and the spike half width, measured at half-maximal amplitude. Control GFP-aGCs N = 11 and Sox11-aGCs N = 9 (4 mice/condition). (**) and (***) denote $p<0.005$ and $p<0.001$. Data are shown as mean ± SEM.

Figure S1. Experimental pipeline and quality control for dataset 1. (A) *Ascl1^{CreERT2};CAG$^{floxStop\text{-}Sun1/sfGFP}$* mice received tamoxifen (TAM) injections to label nuclei from the progeny of RGLs and NPCs. Dentate giri were microdissected at the indicated timepoints (cohorts). Each cohort of GFP$^+$ nuclei was FACS-purified and processed separately using 10x Chromium technology for cDNA library preparation and sequencing. Markers were studied by fluorescence *in situ* hybridizaiton. **(B)** Nuclei composition for each cohort, indicating mice number and sex (F, females; M, males), number of FACS-sorted, and analyzed nuclei. **(C)** FACS sorting of Ruby$^+$/GFP$^+$ nuclei. Scatter plots of ruby dye intensity vs. log(GFP intensity) for purified nuclei isolated at w1, w2, w4 and w8. Green squares highlight the GFP$^+$/Ruby$^+$ population, with thºe number indicating % GFP$^+$

nuclei in the total population. **(D)** Confocal images of FACS-purified Ruby$^+$ nuclei exhibiting GFP anchored to the nuclear membrane. Scale bars: 50 μm (upper panels) and 10 μm (lower panels). **(E)** Quality measurements of snRNA-seq libraries. Scatter plot depicting the number of genes (Features) vs. the number of mRNA molecules (counts) per nuclei for each timepoint. snRNA-seq detected similar number of genes and transcript molecules across cohorts. **(F)** Contribution of timed cohorts to cluster composition.

Figure S2. Quality control and cluster distribution for dataset 2. (A) Nuclei composition for each cohort, indicating mice number and sex (F, females; M, males), number of FACS-sorted, and analyzed nuclei. **(B)** Quality measurements of snRNA-seq libraries. Scatter plot depicting the number of genes (Features) vs. the number of mRNA molecules (counts) per nuclei for each timepoint. snRNA-seq detected similar number of genes and transcript molecules across cohorts. **(C)** mKNN graph displaying cluster identity. **(D)** Progression of each cohort and their localization over the mKNN graph. Nuclei density is indicated by the yellow (low) to red (high) gradient. **(E)** Nuclei distribution in all clusters for each neuronal cohort. **(F)** Contribution of timed cohorts to cluster composition.

Figure S3. Cluster identity and transitions in dataset 2. (A) Violin plot showing the expression level of canonical marker genes for the defined clusters. Note that most identified clusters are conserved with dataset 1, highlighting the reproducibility between experiments. **(B)** Differentially expressed genes (DEGs) between adjacent cluster transitions indicated on top (DEGs listed in **Table S3**). An additional comparison (non-adjacent) is shown on the right. Up- and downregulated genes are shown in red and blue.

Figure S4. Molecular signatures of early stages of adult neurogenesis. (A) Heatmap showing the mean of row-wise normalized expression of canonical cell-cycle markers across clusters. Pseudocolor scale on the right denotes mean expression level. **(B)** Heatmap showing the mean of row-wise normalized expression of top 20 specific upregulated DEGs across clusters. These genes are downregulated after GCimm2. **(C)** Spike plot displaying the mean expression DEGs shown in (B). Nuclei were arranged according to their pseudotime. Black dashes show the mean expression for each cluster. **(D)** Top GO biological processes for the enrichment analysis of DEGs in the transition from NB1 to NB2. FDR cutoff = 0.05 (using ShinyGO 0.77). All data in the figure correspond to dataset 1.

Figure S5. Spatial validation of GCimm1 and GCimm2 markers by RNA in situ hybridization. (A,B) Heatmaps showing the row-wise normalized expression of marker genes for GCimm1 and GCimm2 across clusters (top 50 genes). Marker genes were selected as described in the Methods section. Pseudocolor scales on the right denote mean expression level. Data correspond to dataset 1. **(C)** *In situ* hybridization of dentate gyrus sections from 6/7-week-old mice. Example single plane confocal images. Immature-stage markers were localized near the subgranular zone. DAPI (grey) was used to label cell nuclei. Scale bar, 20 μm.

Figure S6. Switch in biological processes during the exit from immature neuronal stages. (A, B) GO biological processes are shown for the enrichment analysis of the top-50 DEGs in the transition from GCimm2 to GCyoung. FDR cutoff = 0.05 (using ShinyGO 0.77). **(C, D)** Violin plots showing the mean expression levels of DEGs for downregulated **(C)** and upregulated GO terms **(D)** for the defined clusters. All data in the figure correspond to dataset 1.

Figure S7. The GCyoung to GCmat1 transition displays quantitative rather than qualitative changes and reveals nuclei with ventral signature. (A) Volcano plot showing differential expression analysis (FC $\geq$ 1.5 or $\leq$ -1.5 and FDR $\leq$ 0.05) displaying relevant gene examples. **(B)** Violin plots showing the expression level of upregulated DEGs of the GCyoung to GCmat1 transition. **(C)** t-SNE visualization for identified clusters (left panel). Enlarged plot section displaying the GCyoung, GCmat1 and GCmat2 clusters, depicting the mean expression of genes correlated with ventral localization: *Ntm, Trhr, Scn9a, Stk32b, Thsd7b, Cntnap2, Atp2b4 and* Pde1a. All data in the figure correspond to dataset 1.

Figure S8. Pseudotime and density profiles are conserved between datasets. (A) Density distribution of all nuclei along the pseudotime progression for each cohort, comparing datasets 1 and 2. The four cellular states are conserved: 1st RGL; 2nd NPC; 3rd NB1-GCimm1-GCcimm2; 4th GCyoung-GCmat1. Dashed lines depict major transitions along development. Color codes below denote cluster identity. **(B)** Violin plots showing the mean expression levels of *Sox4*, *Sox11* and *Foxo1* regulons for the defined clusters in dataset 1.

ADDITIONAL SUPPLEMENTAL MATERIAL (Excel files)

Table S1. DATASET 1. Top 100 genes with highest variability, corresponding to Figure 1E.

Table S2. DATASET 1. Differentially expressed genes for cluster transitions in dataset 1, corresponding to Figs. 2E; 3B,C,E; 4B,C; S7A.

Table S3. DATASET 2. Differentially expressed genes for cluster transitions in dataset 2, corresponding to Figs. S3B.

Table S4. DATASET 1. Ion channels, neurotransmitter receptors, and molecules involved in synaptic transmission, corresponding to Figure 4D.

Table S5. DATASET 2. Regulons with differential expression between immature and mature aCGs, corresponding to Figure 6D.

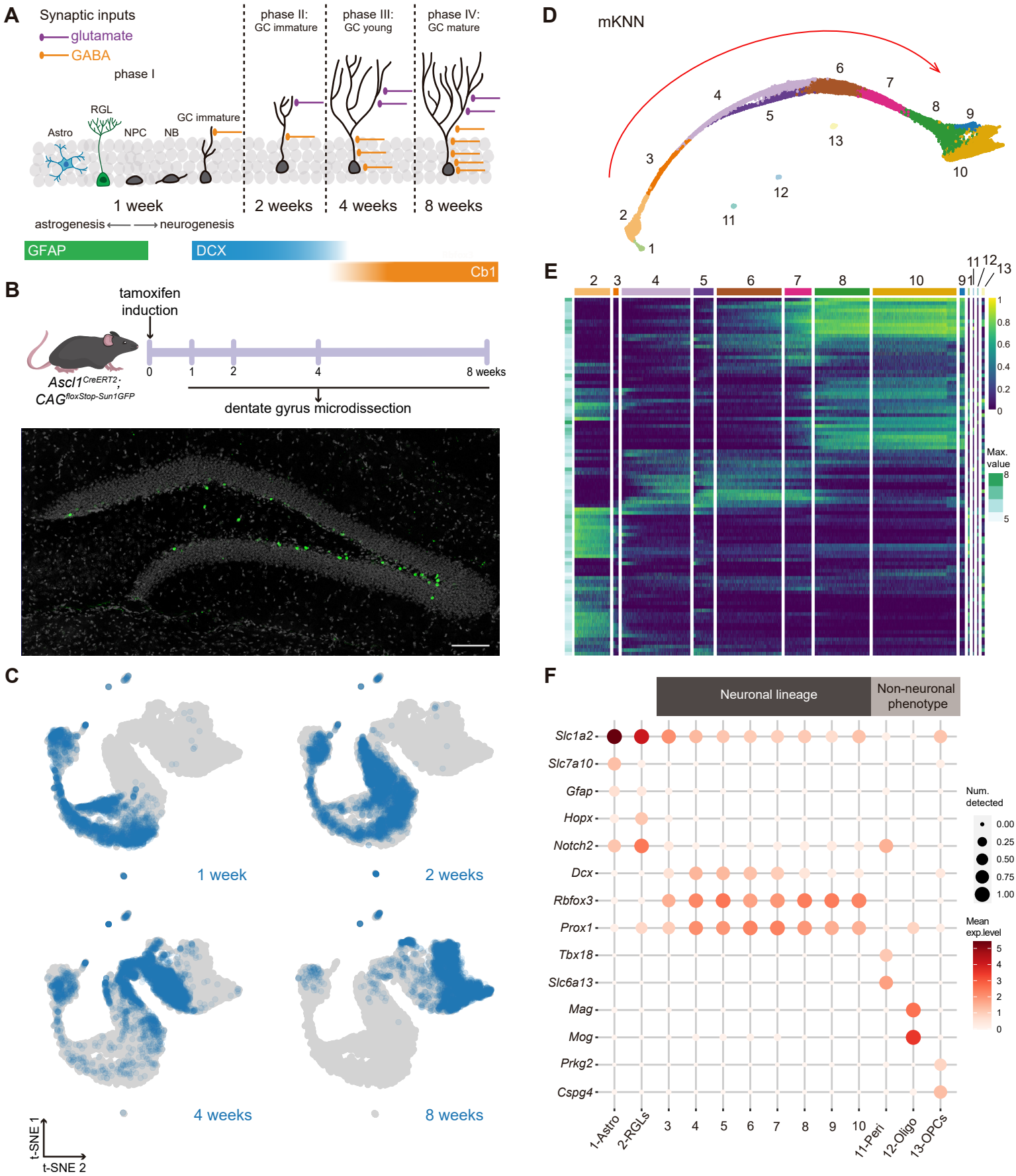
A
Synaptic inputs
glutamate
GABA
phase I
phase II: GC immature
phase III: GC young
phase IV: GC mature
RGL
Astro
NPC
NB
GC immature
1 week
2 weeks
4 weeks
8 weeks
astrogenesis
neurogenesis
GFAP
DCX
Cb1
B
tamoxifen induction
Ascl1CreERT2; CAGfloxStop-Sun1GFP
0
1
2
4
8 weeks
dentate gyrus microdissection
C
1 week
2 weeks
4 weeks
8 weeks
t-SNE 1
t-SNE 2
D
mKNN
1
2
3
4
5
6
7
8
9
10
11
12
13
E
2
3
4
5
6
7
8
10
9
11
12
13
Max. value
F
Neuronal lineage
Non-neuronal phenotype
Slc1a2
Slc7a10
Gfap
Hopx
Notch2
Dcx
Rbfox3
Prox1
Tbx18
Slc6a13
Mag
Mog
Prkg2
Cspg4
1-Astro
2-RGLs
3
4
5
6
7
8
9
10
11-Peri
12-Oligo
13-OPCs
Num. detected
0.00
0.25
0.50
0.75
1.00
Mean exp.level

Figure 1

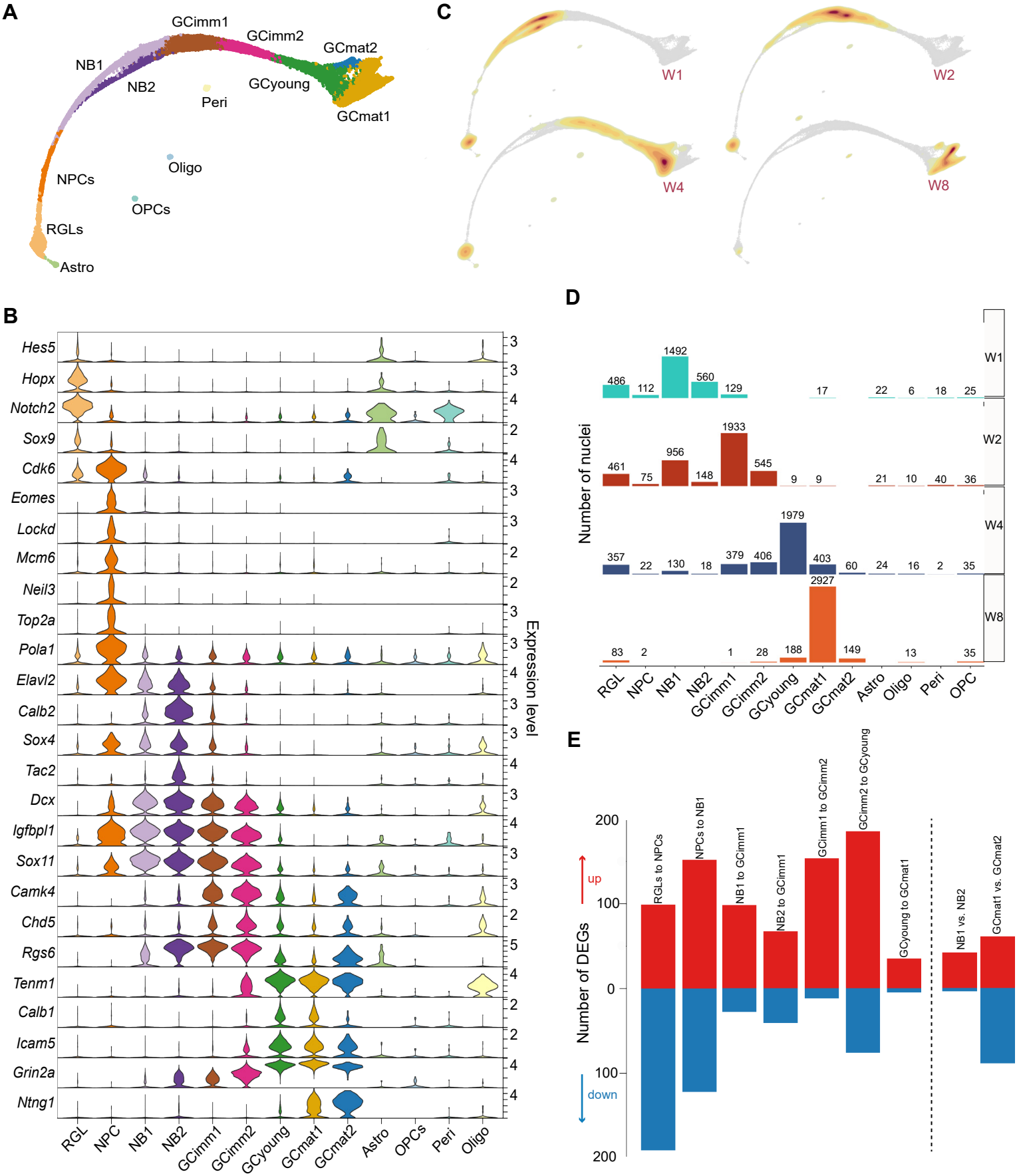
A
GCimm1
GCimm2
GCmat2
NB1
NB2
GCyoung
Peri
GCmat1
Oligo
NPCs
OPCs
RGLs
Astro
C
W1
W2
W4
W8
B
Hes5
Hopx
Notch2
Sox9
Cdk6
Eomes
Lockd
Mcm6
Neil3
Top2a
Pola1
Elavl2
Calb2
Sox4
Tac2
Dcx
Igfbpl1
Sox11
Camk4
Chd5
Rgs6
Tenm1
Calb1
Icam5
Grin2a
Ntng1
RGL
NPC
NB1
NB2
GCimm1
GCimm2
GCyoung
GCmat1
GCmat2
Astro
OPCs
Peri
Oligo
Expression level
D
Number of nuclei
W1
W2
W4
W8
RGL
NPC
NB1
NB2
GCimm1
GCimm2
GCyoung
GCmat1
GCmat2
Astro
Oligo
Peri
OPC
E
Number of DEGs
up
down
RGLs to NPCs
NPCs to NB1
NB1 to GCimm1
NB2 to GCimm1
GCimm1 to GCimm2
GCimm2 to GCyoung
GCyoung to GCmat1
NB1 vs. NB2
GCmat1 vs. GCmat2

Figure 2

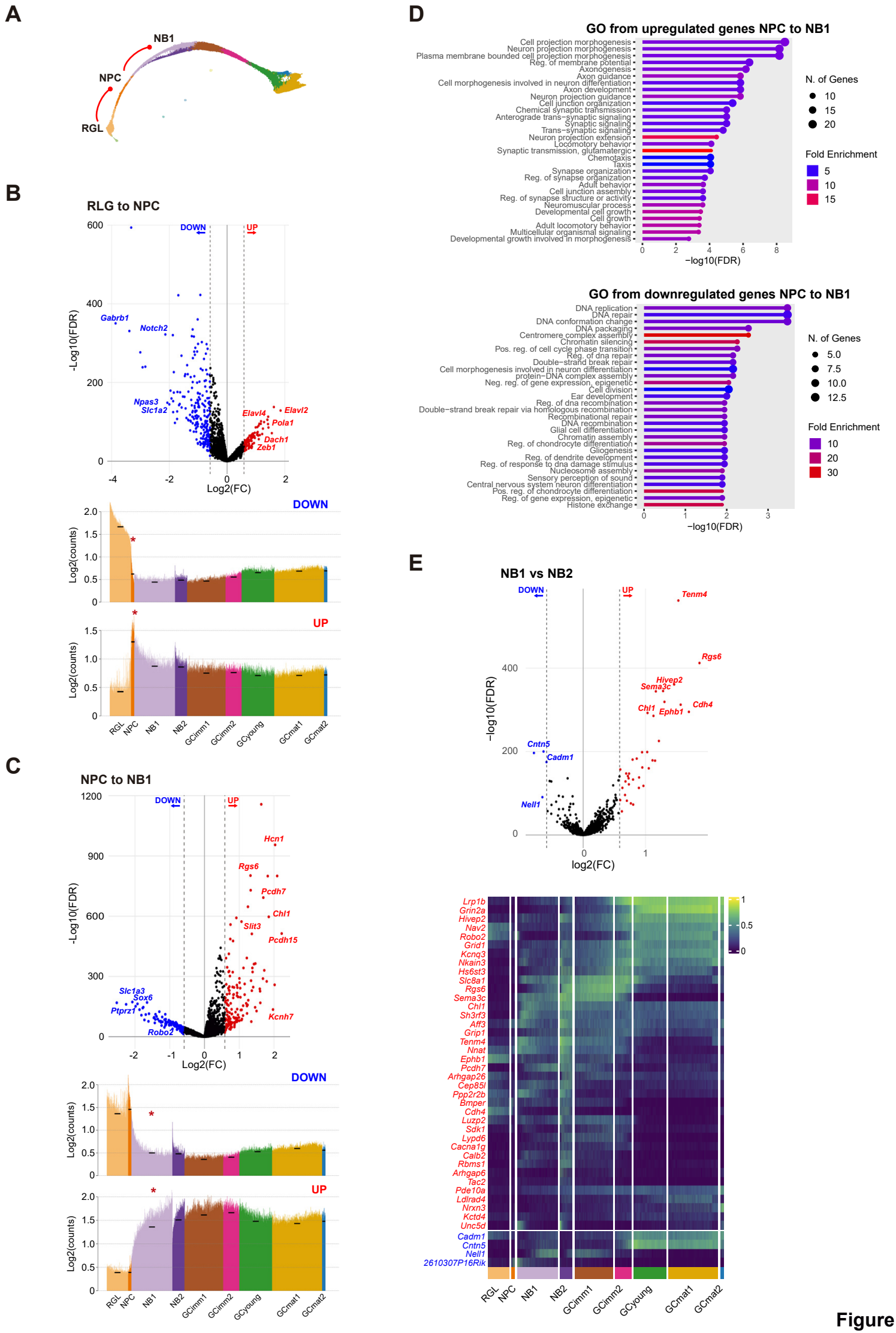
A
NB1
NPC
RGL
B
RLG to NPC
DOWN
UP
-Log10(FDR)
Log2(FC)
Gabrb1
Notch2
Npas3
Slc1a2
Elavl4
Elavl2
Pola1
Dach1
Zeb1
Log2(counts)
RGL
NPC
NB1
NB2
GCimm1
GCimm2
GCyoung
GCmat1
GCmat2
C
NPC to NB1
Hcn1
Rgs6
Pcdh7
Chl1
Slit3
Pcdh15
Kcnh7
Slc1a3
Sox6
Ptprz1
Robo2
D
GO from upregulated genes NPC to NB1
Cell projection morphogenesis
Neuron projection morphogenesis
Plasma membrane bounded cell projection morphogenesis
Reg. of membrane potential
Axonogenesis
Axon guidance
Cell morphogenesis involved in neuron differentiation
Axon development
Neuron projection guidance
Cell junction organization
Chemical synaptic transmission
Anterograde trans−synaptic signaling
Synaptic signaling
Trans−synaptic signaling
Neuron projection extension
Locomotory behavior
Synaptic transmission, glutamatergic
Chemotaxis
Taxis
Synapse organization
Reg. of synapse organization
Adult behavior
Cell junction assembly
Reg. of synapse structure or activity
Neuromuscular process
Developmental cell growth
Cell growth
Adult locomotory behavior
Multicellular organismal signaling
Developmental growth involved in morphogenesis
−log10(FDR)
N. of Genes
10
15
20
Fold Enrichment
5
10
15
GO from downregulated genes NPC to NB1
DNA replication
DNA repair
DNA conformation change
DNA packaging
Centromere complex assembly
Chromatin silencing
Pos. reg. of cell cycle phase transition
Reg. of dna repair
Double−strand break repair
Cell morphogenesis involved in neuron differentiation
protein−DNA complex assembly
Neg. reg. of gene expression, epigenetic
Cell division
Ear development
Reg. of dna recombination
Double−strand break repair via homologous recombination
Recombinational repair
DNA recombination
Glial cell differentiation
Chromatin assembly
Reg. of chondrocyte differentiation
Gliogenesis
Reg. of dendrite development
Reg. of response to dna damage stimulus
Nucleosome assembly
Sensory perception of sound
Central nervous system neuron differentiation
Pos. reg. of chondrocyte differentiation
Reg. of gene expression, epigenetic
Histone exchange
−log10(FDR)
N. of Genes
5.0
7.5
10.0
12.5
Fold Enrichment
10
20
30
E
NB1 vs NB2
DOWN
UP
Tenm4
Rgs6
Hivep2
Sema3c
Chl1
Ephb1
Cdh4
Cntn5
Cadm1
Nell1
−log10(FDR)
log2(FC)
Lrp1b
Grin2a
Hivep2
Nav2
Robo2
Grid1
Kcnq3
Nkain3
Hs6st3
Slc8a1
Rgs6
Sema3c
Chl1
Sh3rf3
Aff3
Grip1
Tenm4
Nnat
Ephb1
Pcdh7
Arhgap26
Cep85l
Ppp2r2b
Bmper
Cdh4
Luzp2
Sdk1
Lypd6
Cacna1g
Calb2
Rbms1
Arhgap6
Tac2
Pde10a
Ldlrad4
Nrxn3
Kctd4
Unc5d
Cadm1
Cntn5
Nell1
2610307P16Rik
RGL
NPC
NB1
NB2
GCimm1
GCimm2
GCyoung
GCmat1
GCmat2

Figure 3

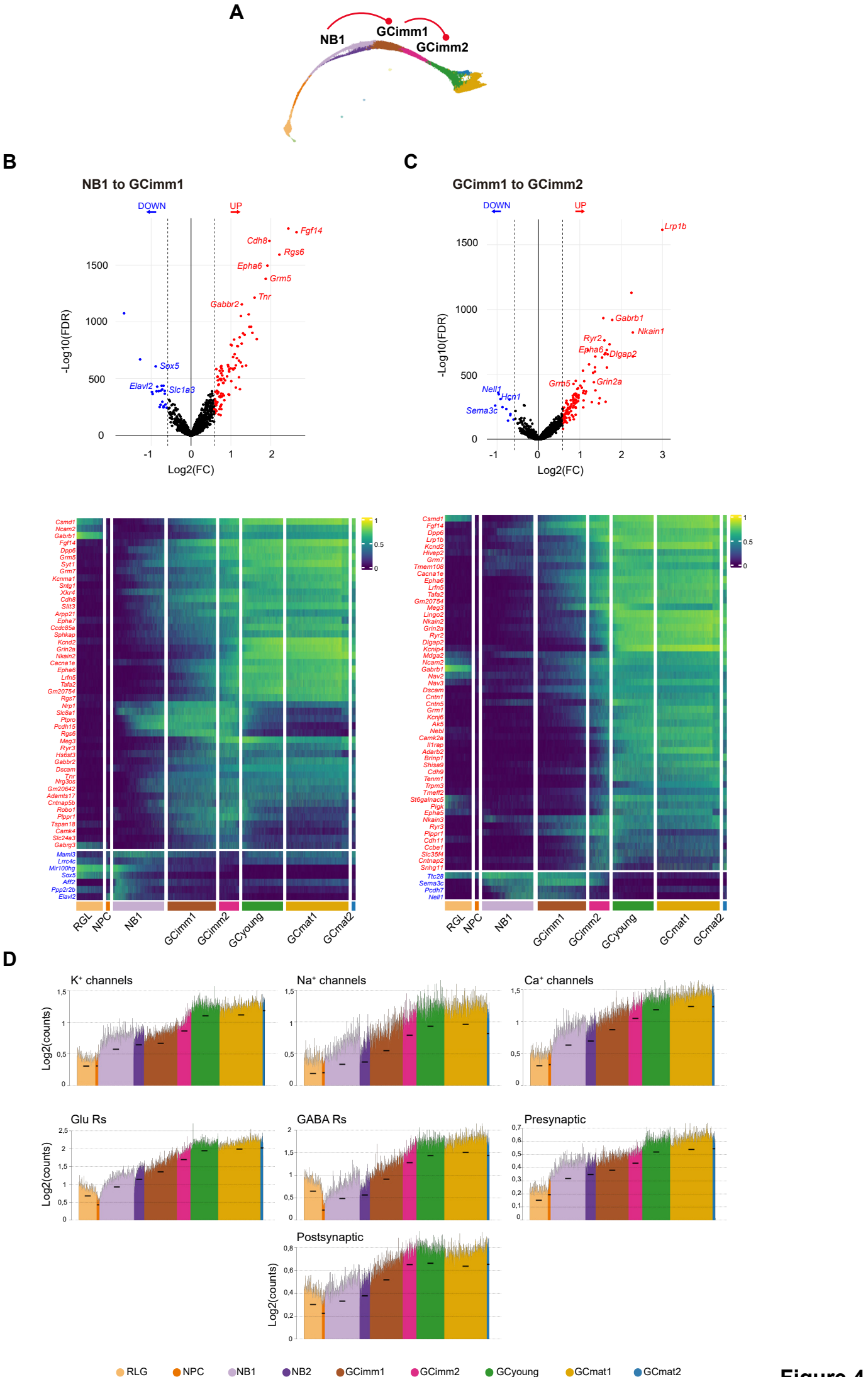
A
NB1
GCimm1
GCimm2
B
NB1 to GCimm1
DOWN
UP
-Log10(FDR)
Log2(FC)
Fgf14
Cdh8
Rgs6
Epha6
Grm5
Tnr
Gabbr2
Sox5
Elavl2
Slc1a3
C
GCimm1 to GCimm2
Lrp1b
Gabrb1
Nkain1
Ryr2
Epha6
Dlgap2
Grin2a
Grm5
Nell1
Hcn1
Sema3c
RGL
NPC
NB1
GCimm1
GCimm2
GCyoung
GCmat1
GCmat2
D
K⁺ channels
Na⁺ channels
Ca⁺ channels
Glu Rs
GABA Rs
Presynaptic
Postsynaptic
Log2(counts)
RLG
NPC
NB1
NB2
GCimm1
GCimm2
GCyoung
GCmat1
GCmat2

Figure 4

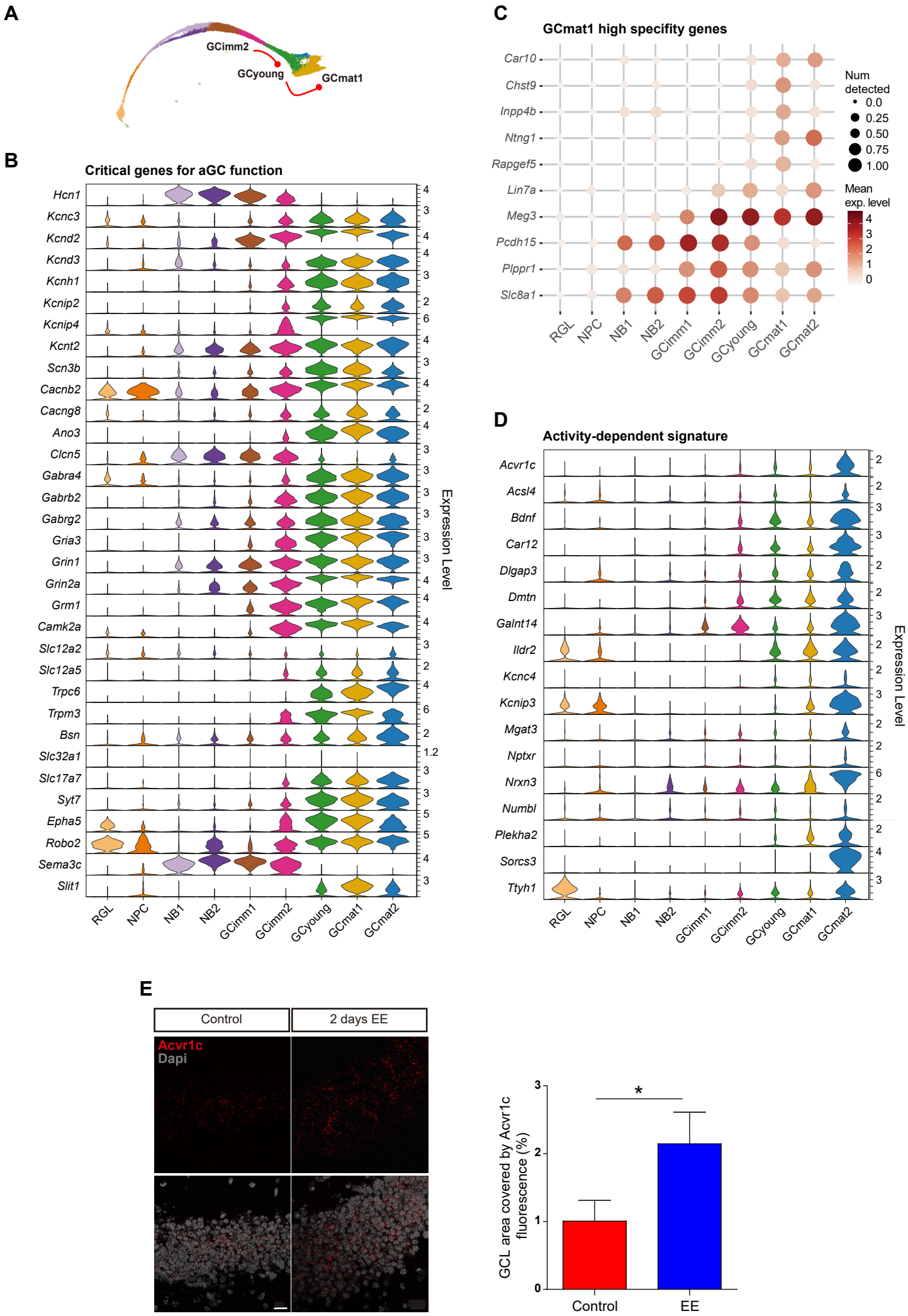
A
GCimm2
GCyoung
GCmat1
B
Critical genes for aGC function
Hcn1
Kcnc3
Kcnd2
Kcnd3
Kcnh1
Kcnip2
Kcnip4
Kcnt2
Scn3b
Cacnb2
Cacng8
Ano3
Clcn5
Gabra4
Gabrb2
Gabrg2
Gria3
Grin1
Grin2a
Grm1
Camk2a
Slc12a2
Slc12a5
Trpc6
Trpm3
Bsn
Slc32a1
Slc17a7
Syt7
Epha5
Robo2
Sema3c
Slit1
RGL
NPC
NB1
NB2
GCimm1
GCimm2
GCyoung
GCmat1
GCmat2
Expression Level
C
GCmat1 high specifity genes
Car10
Chst9
Inpp4b
Ntng1
Rapgef5
Lin7a
Meg3
Pcdh15
Plppr1
Slc8a1
Num detected
0.0
0.25
0.50
0.75
1.00
Mean exp. level
D
Activity-dependent signature
Acvr1c
Acsl4
Bdnf
Car12
Dlgap3
Dmtn
Galnt14
Ildr2
Kcnc4
Kcnip3
Mgat3
Nptxr
Nrxn3
Numbl
Plekha2
Sorcs3
Ttyh1
Expression Level
E
Control
2 days EE
Acvr1c
Dapi
GCL area covered by Acvr1c fluorescence (%)
Control
EE
*

Figure 5

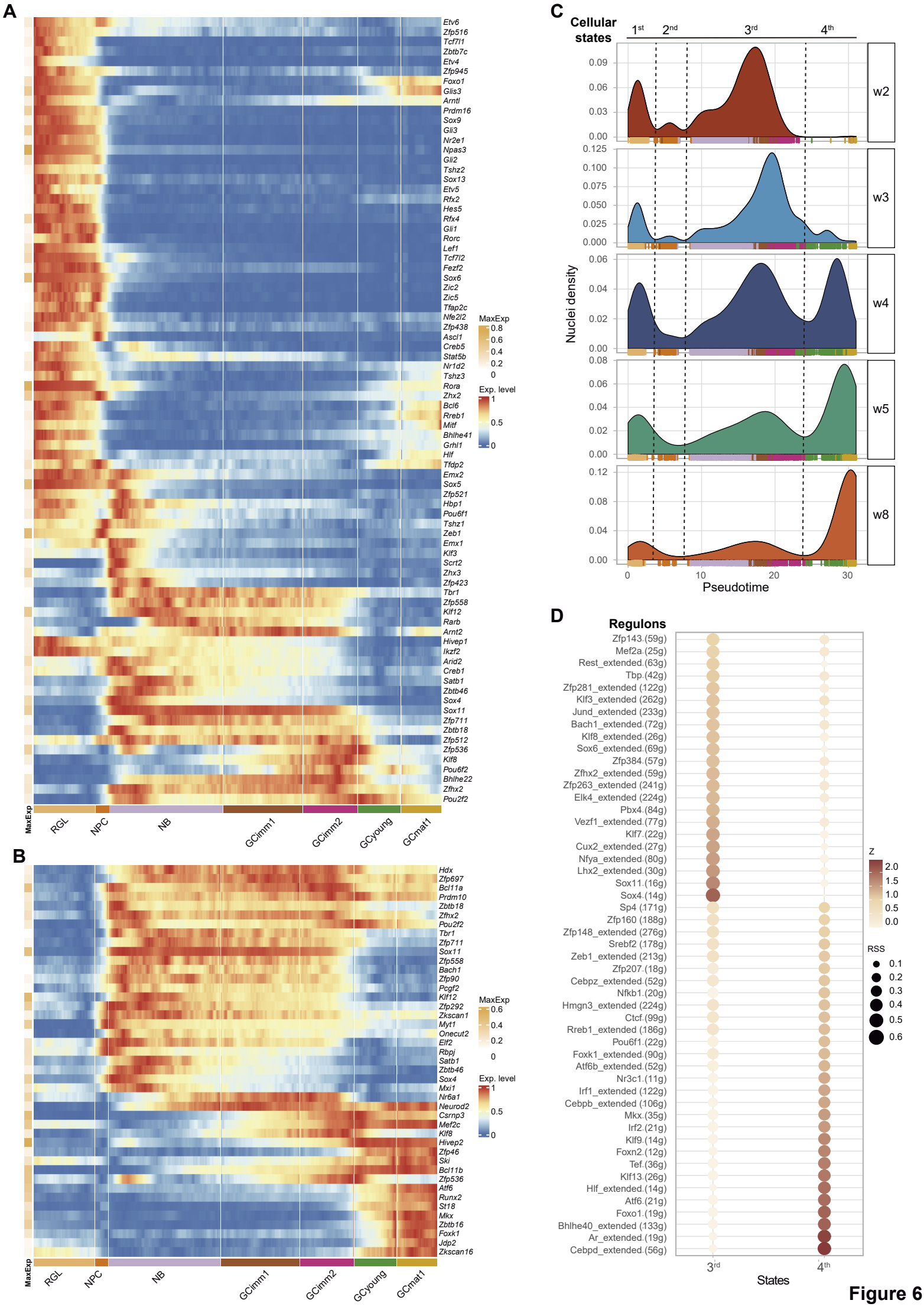
A
Etv6
Zfp516
Tcf7l1
Zbtb7c
Etv4
Zfp945
Foxo1
Glis3
Arntl
Prdm16
Sox9
Gli3
Nr2e1
Npas3
Gli2
Tshz2
Sox13
Etv5
Rfx2
Hes5
Rfx4
Gli1
Rorc
Lef1
Tcf7l2
Fezf2
Sox6
Zic2
Zic5
Tfap2c
Nfe2l2
Zfp438
Ascl1
Creb5
Stat5b
Nr1d2
Tshz3
Rora
Zhx2
Bcl6
Rreb1
Mitf
Bhlhe41
Grhl1
Hlf
Tfdp2
Emx2
Sox5
Zfp521
Hbp1
Pou6f1
Tshz1
Zeb1
Emx1
Klf3
Scrt2
Zhx3
Zfp423
Tbr1
Zfp558
Klf12
Rarb
Arnt2
Hivep1
Ikzf2
Arid2
Creb1
Satb1
Zbtb46
Sox4
Sox11
Zfp711
Zbtb18
Zfp512
Zfp536
Klf8
Pou6f2
Bhlhe22
Zfhx2
Pou2f2
MaxExp
0.8
0.6
0.4
0.2
0
Exp. level
1
0.5
0
MaxExp
RGL
NPC
NB
GCimm1
GCimm2
GCyoung
GCmat1
B
Hdx
Zfp697
Bcl11a
Prdm10
Zbtb18
Zfhx2
Pou2f2
Tbr1
Zfp711
Sox11
Zfp558
Bach1
Zfp90
Pcgf2
Klf12
Zfp292
Zkscan1
Myt1
Onecut2
Elf2
Rbpj
Satb1
Zbtb46
Sox4
Mxi1
Nr6a1
Neurod2
Csrnp3
Mef2c
Klf8
Hivep2
Zfp46
Ski
Bcl11b
Zfp536
Atf6
Runx2
St18
Mkx
Zbtb16
Foxk1
Jdp2
Zkscan16
MaxExp
0.6
0.4
0.2
0
Exp. level
1
0.5
0
MaxExp
RGL
NPC
NB
GCimm1
GCimm2
GCyoung
GCmat1
C
Cellular states
1st
2nd
3rd
4th
w2
w3
w4
w5
w8
Nuclei density
Pseudotime
D
Regulons
Zfp143 (59g)
Mef2a (25g)
Rest_extended (63g)
Tbp (42g)
Zfp281_extended (122g)
Klf3_extended (262g)
Jund_extended (233g)
Bach1_extended (72g)
Klf8_extended (26g)
Sox6_extended (69g)
Zfp384 (57g)
Zfhx2_extended (59g)
Zfp263_extended (241g)
Elk4_extended (224g)
Pbx4 (84g)
Vezf1_extended (77g)
Klf7 (22g)
Cux2_extended (27g)
Nfya_extended (80g)
Lhx2_extended (30g)
Sox11 (16g)
Sox4 (14g)
Sp4 (171g)
Zfp160 (188g)
Zfp148_extended (276g)
Srebf2 (178g)
Zeb1_extended (213g)
Zfp207 (18g)
Cebpz_extended (52g)
Nfkb1 (20g)
Hmgn3_extended (224g)
Ctcf (99g)
Rreb1_extended (186g)
Pou6f1 (22g)
Foxk1_extended (90g)
Atf6b_extended (52g)
Nr3c1 (11g)
Irf1_extended (122g)
Cebpb_extended (106g)
Mkx (35g)
Irf2 (21g)
Klf9 (14g)
Foxn2 (12g)
Tef (36g)
Klf13 (26g)
Hlf_extended (14g)
Atf6 (21g)
Foxo1 (19g)
Bhlhe40_extended (133g)
Ar_extended (19g)
Cebpd_extended (56g)
3rd
4th
States
Z
2.0
1.5
1.0
0.5
0.0
RSS
0.1
0.2
0.3
0.4
0.5
0.6

Figure 6

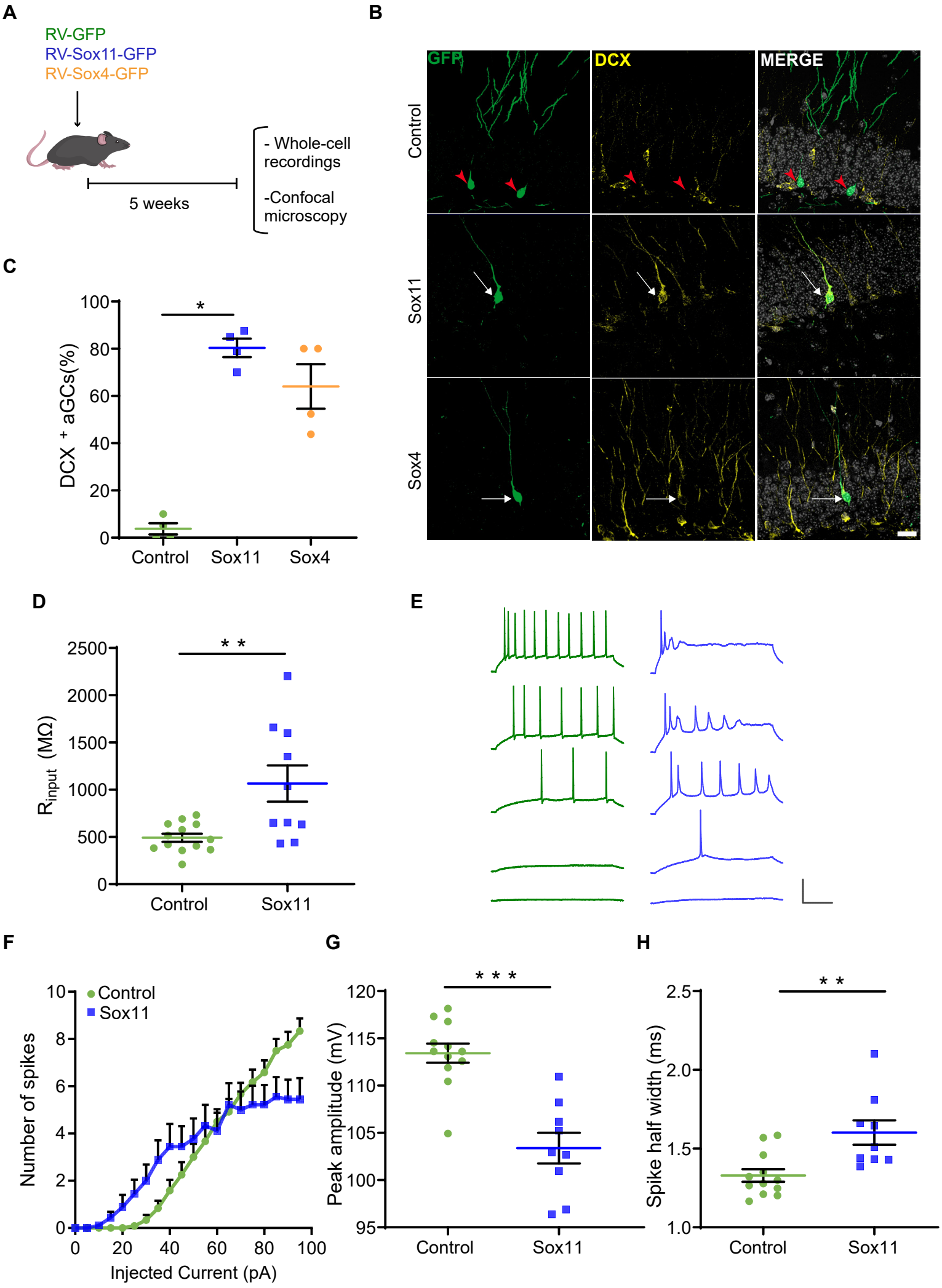
A
RV-GFP
RV-Sox11-GFP
RV-Sox4-GFP
5 weeks
- Whole-cell recordings
-Confocal microscopy
B
GFP
DCX
MERGE
Control
Sox11
Sox4
C
DCX + aGCs(%)
Control
Sox11
Sox4
D
R_{input} (MΩ)
Control
Sox11
E
F
Control
Sox11
Number of spikes
Injected Current (pA)
G
Peak amplitude (mV)
Control
Sox11
H
Spike half width (ms)
Control
Sox11

Figure 7

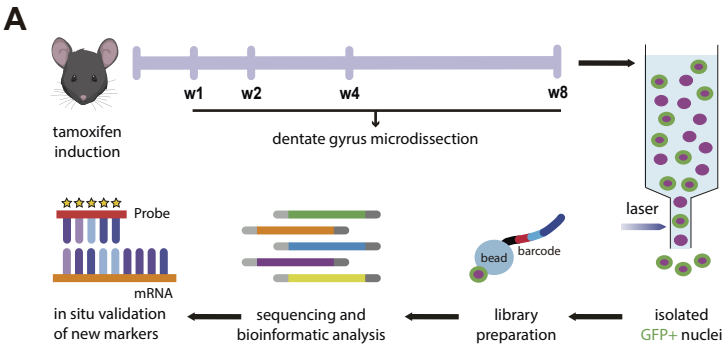

B

Time points	# mice	sex	# FACS events	# nuclei
w1	4	F, M	8300	2867
w2	4	F, M	18000	4243
w4	4	F, M	20000	3831
w8	4	F, M	11374	3426
Total				14367

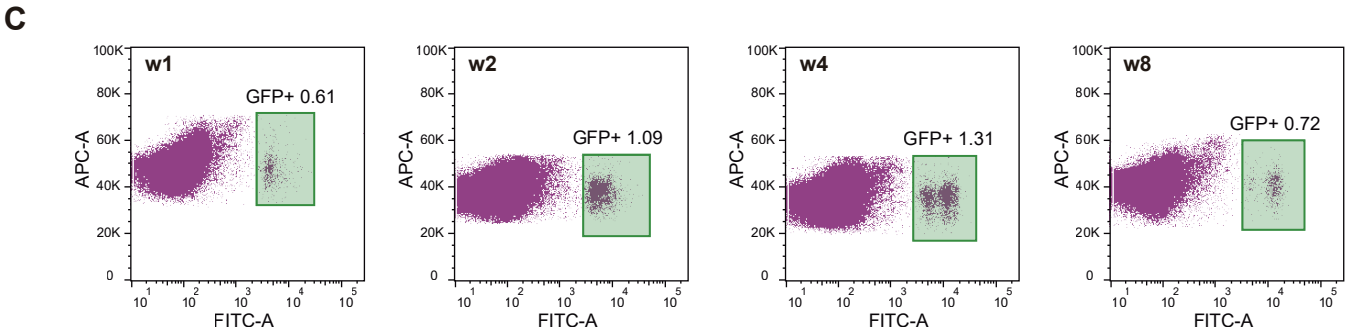

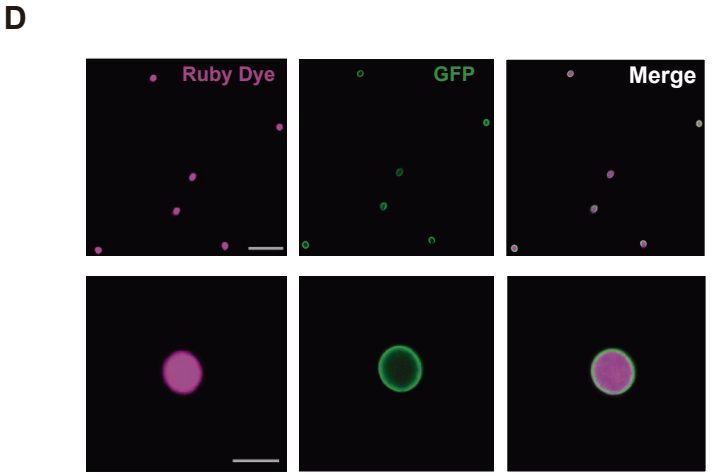

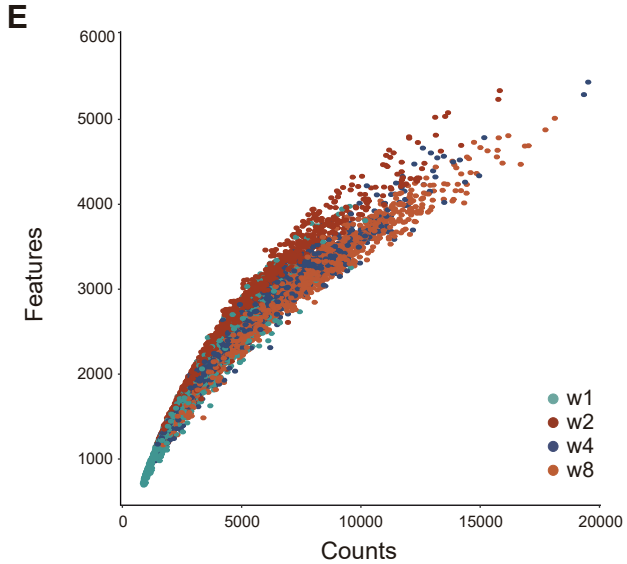

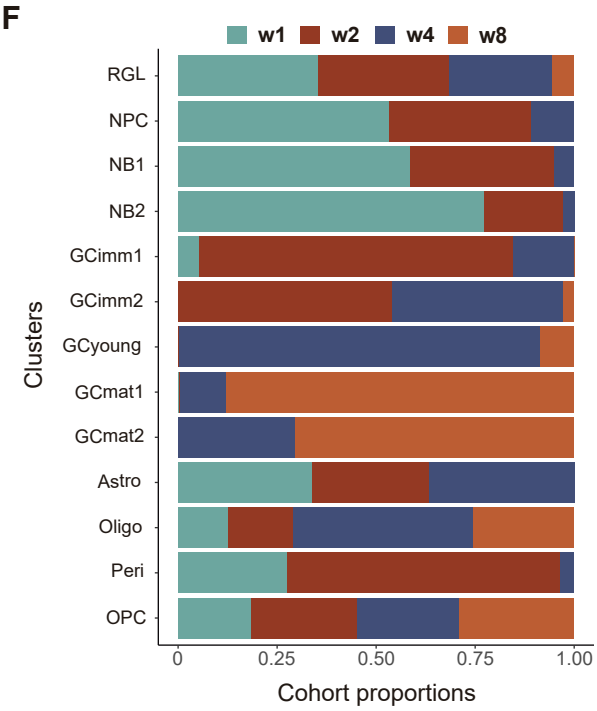

Figure S1

A

Time points	# mice	sex	# FACS events	# nuclei
w2	4	F, M	24090	7685
w3	4	F, M	15861	4975
w4	4	F, M	25628	7498
w5	4	F, M	10000	3139
w8	4	F, M	17511	3419
Total				26716

B

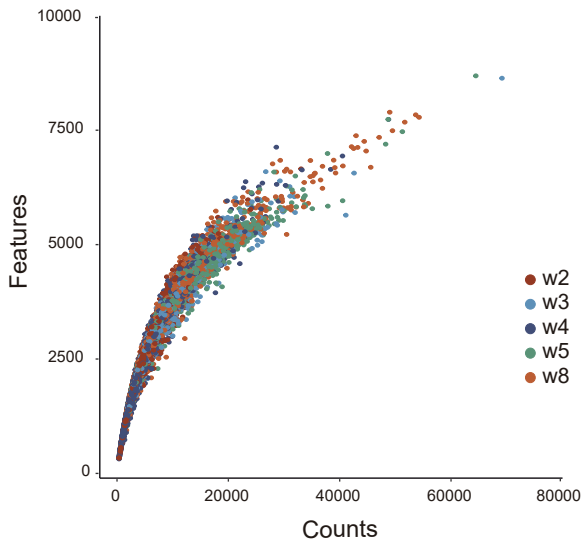

C

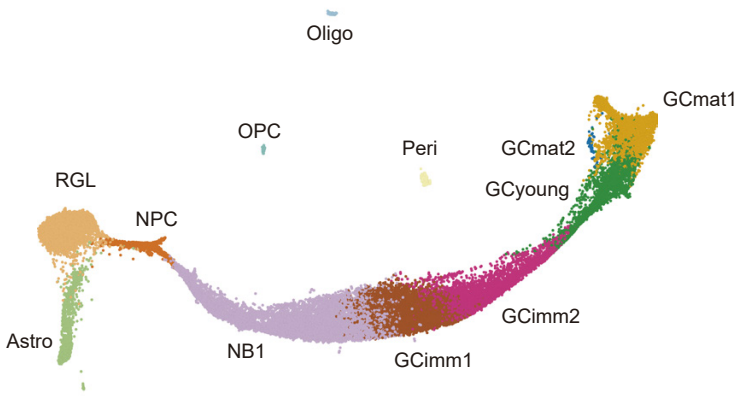

D

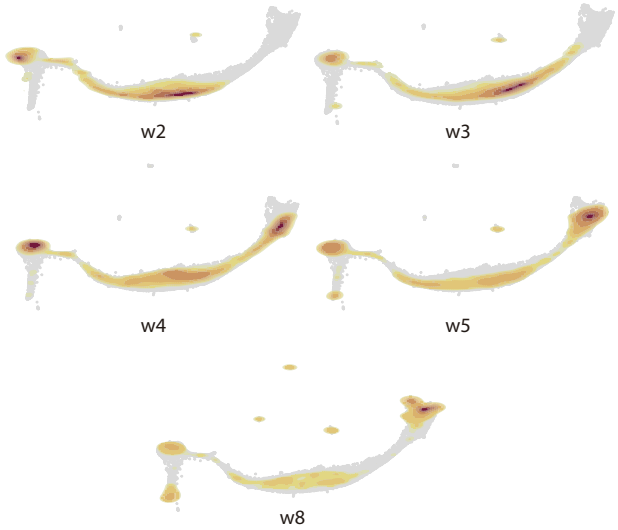

E

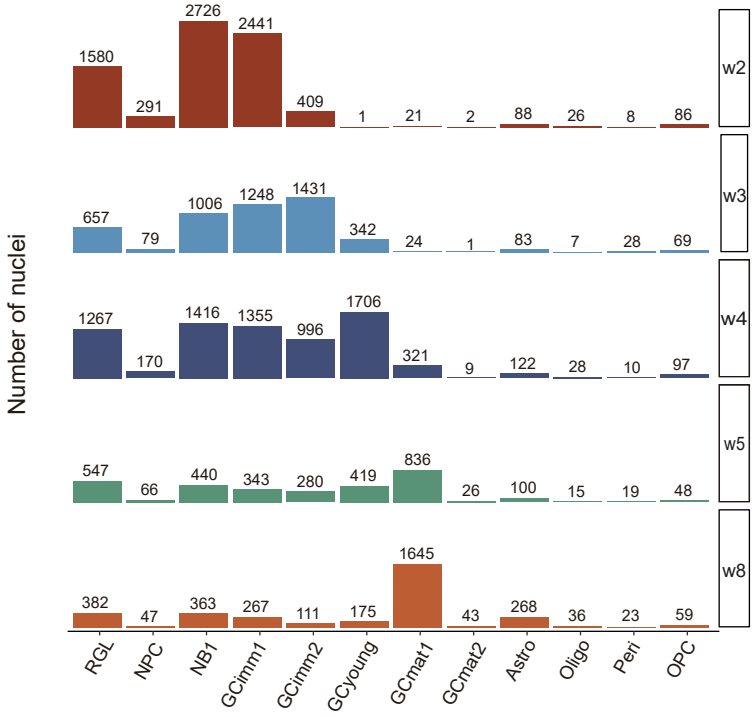

F

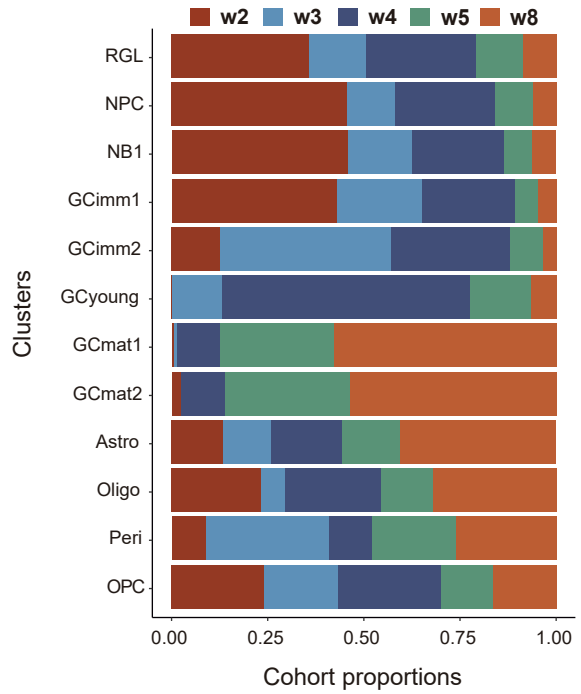

Figure S2

A

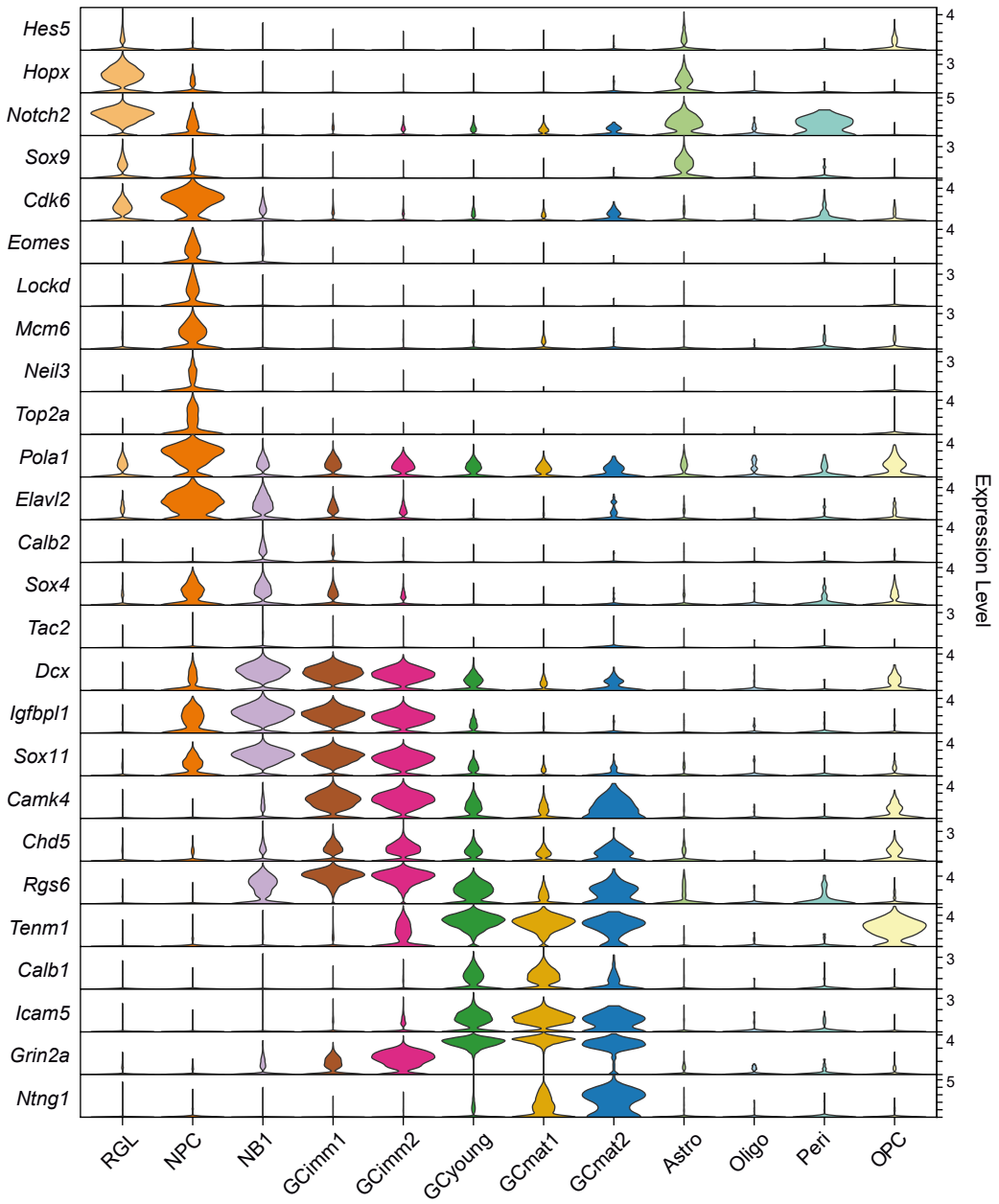
Hes5
Hopx
Notch2
Sox9
Cdk6
Eomes
Lockd
Mcm6
Neil3
Top2a
Pola1
Elavl2
Calb2
Sox4
Tac2
Dcx
Igfbpl1
Sox11
Camk4
Chd5
Rgs6
Tenm1
Calb1
Icam5
Grin2a
Ntng1
RGL
NPC
NB1
GCimm1
GCimm2
GCyoung
GCmat1
GCmat2
Astro
Oligo
Peri
OPC
Expression Level

B

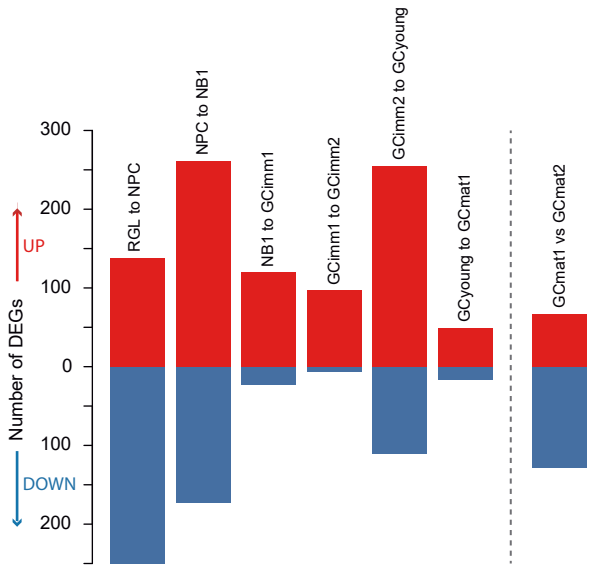
RGL to NPC
NPC to NB1
NB1 to GCimm1
GCimm1 to GCimm2
GCimm2 to GCyoung
GCyoung to GCmat1
GCmat1 vs GCmat2
Number of DEGs
UP
DOWN
300
200
100
0
100
200

Figure S3

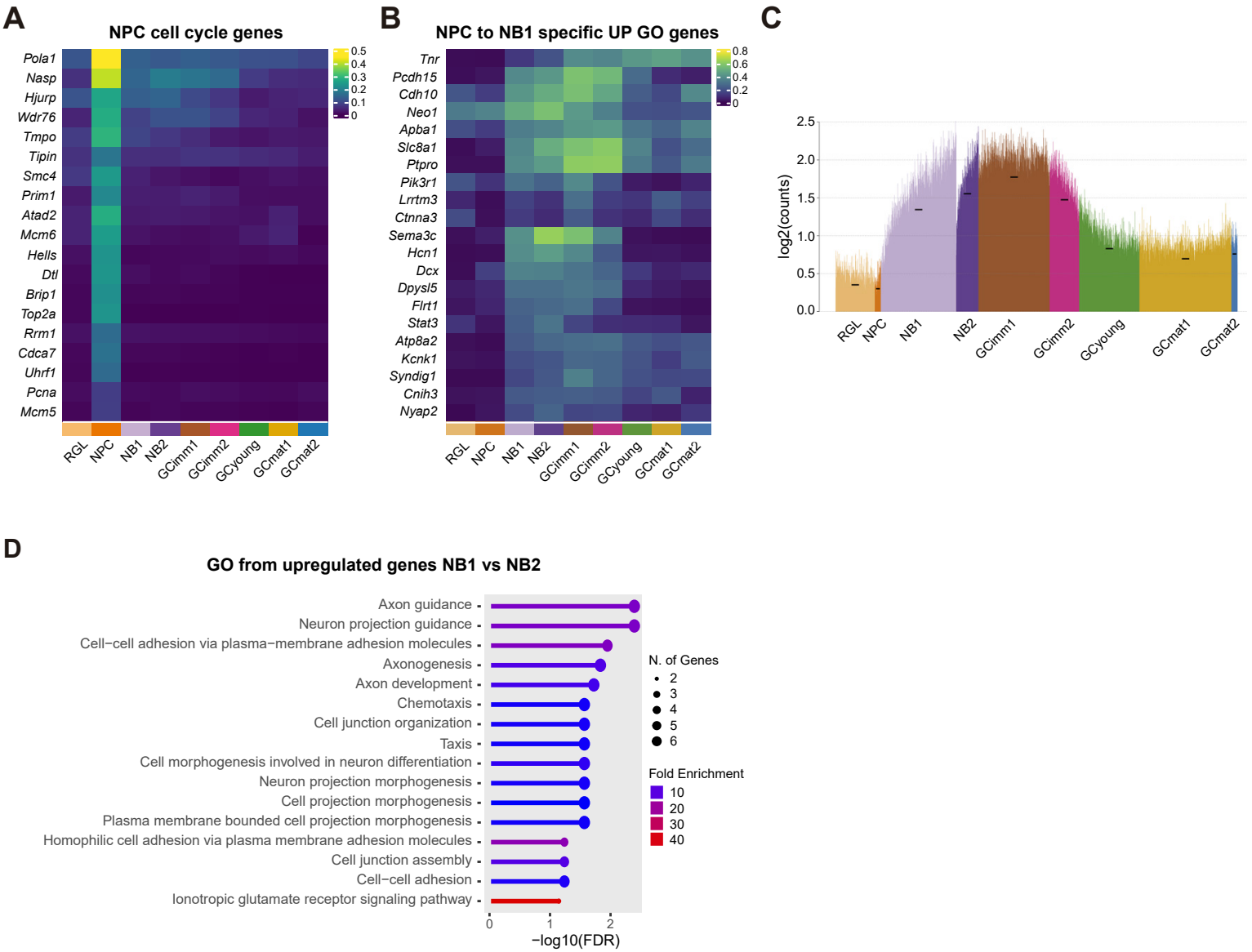
A
NPC cell cycle genes
Pola1
Nasp
Hjurp
Wdr76
Tmpo
Tipin
Smc4
Prim1
Atad2
Mcm6
Hells
Dtl
Brip1
Top2a
Rrm1
Cdca7
Uhrf1
Pcna
Mcm5
0.5
0.4
0.3
0.2
0.1
0
RGL
NPC
NB1
NB2
GCimm1
GCimm2
GCyoung
GCmat1
GCmat2
B
NPC to NB1 specific UP GO genes
Tnr
Pcdh15
Cdh10
Neo1
Apba1
Slc8a1
Ptpro
Pik3r1
Lrrtm3
Ctnna3
Sema3c
Hcn1
Dcx
Dpysl5
Flrt1
Stat3
Atp8a2
Kcnk1
Syndig1
Cnih3
Nyap2
0.8
0.6
0.4
0.2
0
RGL
NPC
NB1
NB2
GCimm1
GCimm2
GCyoung
GCmat1
GCmat2
C
log2(counts)
2.5
2.0
1.5
1.0
0.5
0.0
RGL
NPC
NB1
NB2
GCimm1
GCimm2
GCyoung
GCmat1
GCmat2
D
GO from upregulated genes NB1 vs NB2
Axon guidance
Neuron projection guidance
Cell−cell adhesion via plasma−membrane adhesion molecules
Axonogenesis
Axon development
Chemotaxis
Cell junction organization
Taxis
Cell morphogenesis involved in neuron differentiation
Neuron projection morphogenesis
Cell projection morphogenesis
Plasma membrane bounded cell projection morphogenesis
Homophilic cell adhesion via plasma membrane adhesion molecules
Cell junction assembly
Cell−cell adhesion
Ionotropic glutamate receptor signaling pathway
0
1
2
−log10(FDR)
N. of Genes
2
3
4
5
6
Fold Enrichment
10
20
30
40

Figure S4

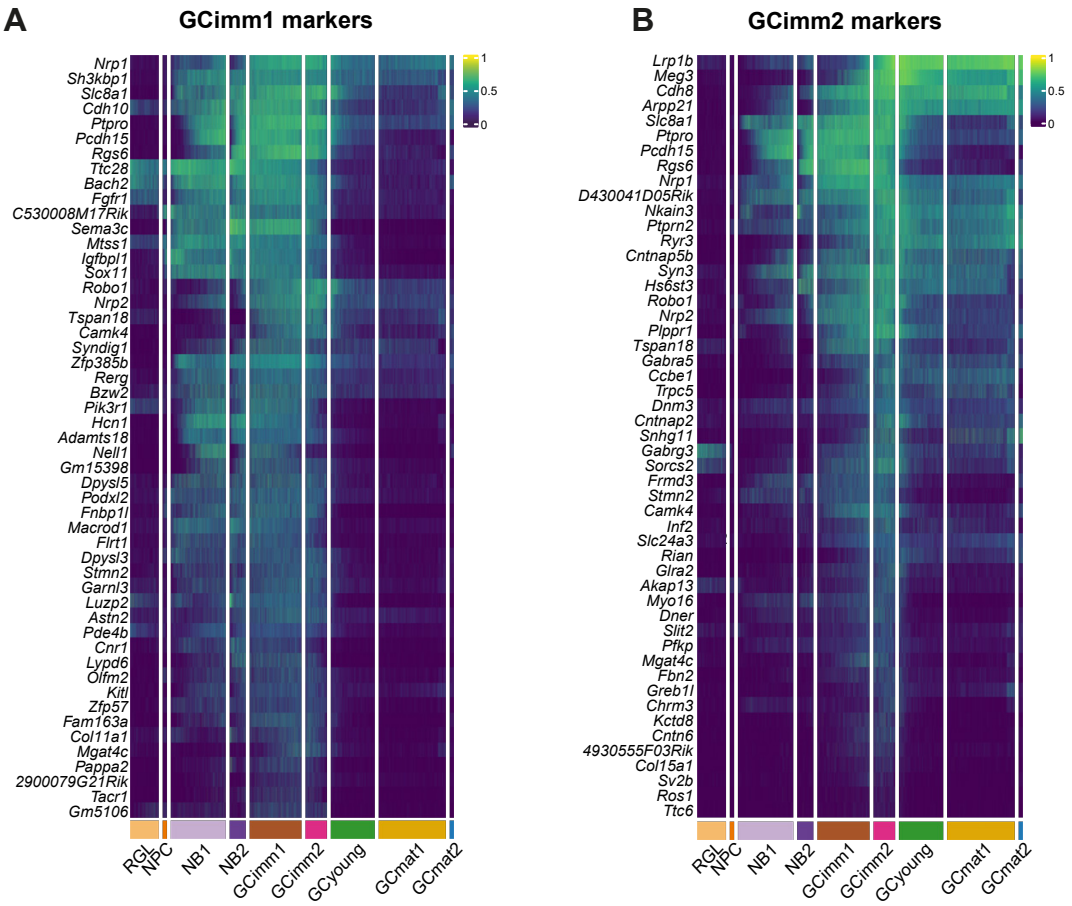
A
GCimm1 markers
Nrp1
Sh3kbp1
Slc8a1
Cdh10
Ptpro
Pcdh15
Rgs6
Ttc28
Bach2
Fgfr1
C530008M17Rik
Sema3c
Mtss1
Igfbpl1
Sox11
Robo1
Nrp2
Tspan18
Camk4
Syndig1
Zfp385b
Rerg
Bzw2
Pik3r1
Hcn1
Adamts18
Nell1
Gm15398
Dpysl5
Podxl2
Fnbp1l
Macrod1
Flrt1
Dpysl3
Stmn2
Garnl3
Luzp2
Astn2
Pde4b
Cnr1
Lypd6
Olfm2
Kitl
Zfp57
Fam163a
Col11a1
Mgat4c
Pappa2
2900079G21Rik
Tacr1
Gm5106
1
0.5
0
RGL
NPC
NB1
NB2
GCimm1
GCimm2
GCyoung
GCmat1
GCmat2
B
GCimm2 markers
Lrp1b
Meg3
Cdh8
Arpp21
Slc8a1
Ptpro
Pcdh15
Rgs6
Nrp1
D430041D05Rik
Nkain3
Ptprn2
Ryr3
Cntnap5b
Syn3
Hs6st3
Robo1
Nrp2
Plppr1
Tspan18
Gabra5
Ccbe1
Trpc5
Dnm3
Cntnap2
Snhg11
Gabrg3
Sorcs2
Frmd3
Stmn2
Camk4
Inf2
Slc24a3
Rian
Glra2
Akap13
Myo16
Dner
Slit2
Pfkp
Mgat4c
Fbn2
Greb1l
Chrm3
Kctd8
Cntn6
4930555F03Rik
Col15a1
Sv2b
Ros1
Ttc6
1
0.5
0
RGL
NPC
NB1
NB2
GCimm1
GCimm2
GCyoung
GCmat1
GCmat2

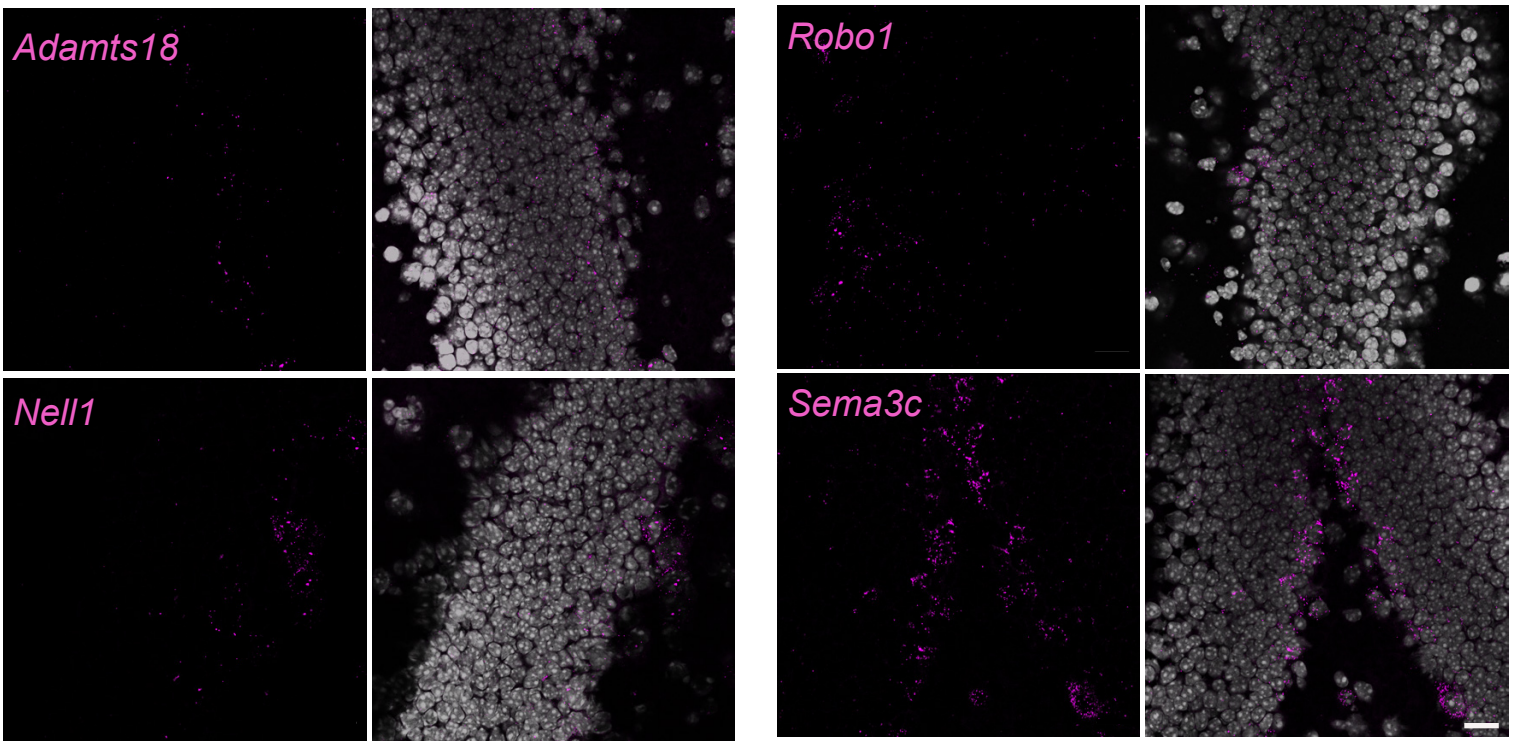
C
Adamts18
Robo1
Nell1
Sema3c

Figure S5

A Downregulated GO terms GCimm2 to GCyoung

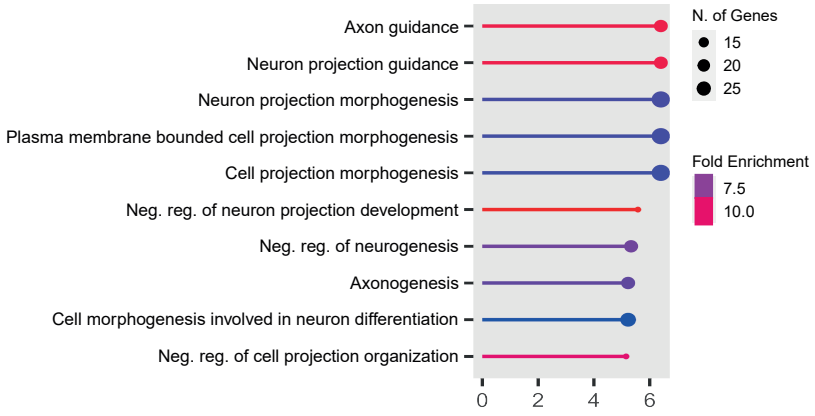

B Upregulated GO terms GCimm2 to GCyoung

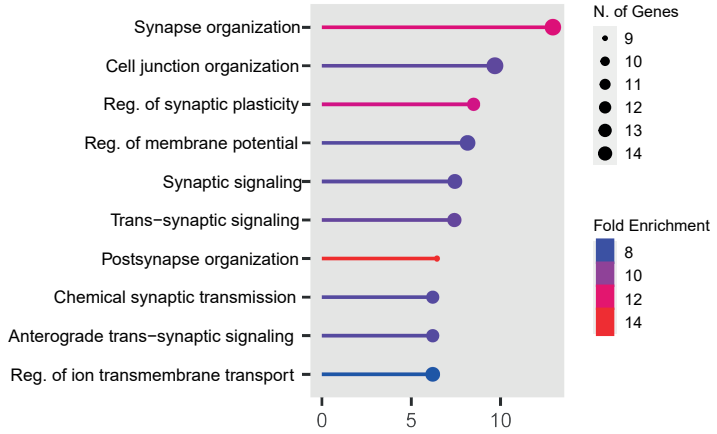

C Downregulated DEGs defining GO terms

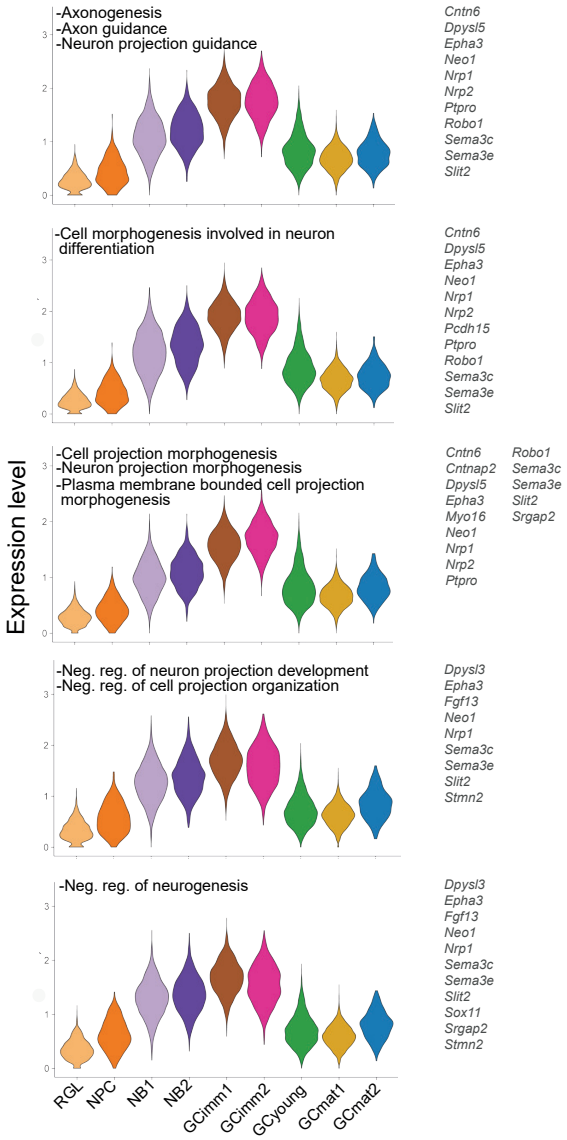

D Upregulated DEGs defining GO terms

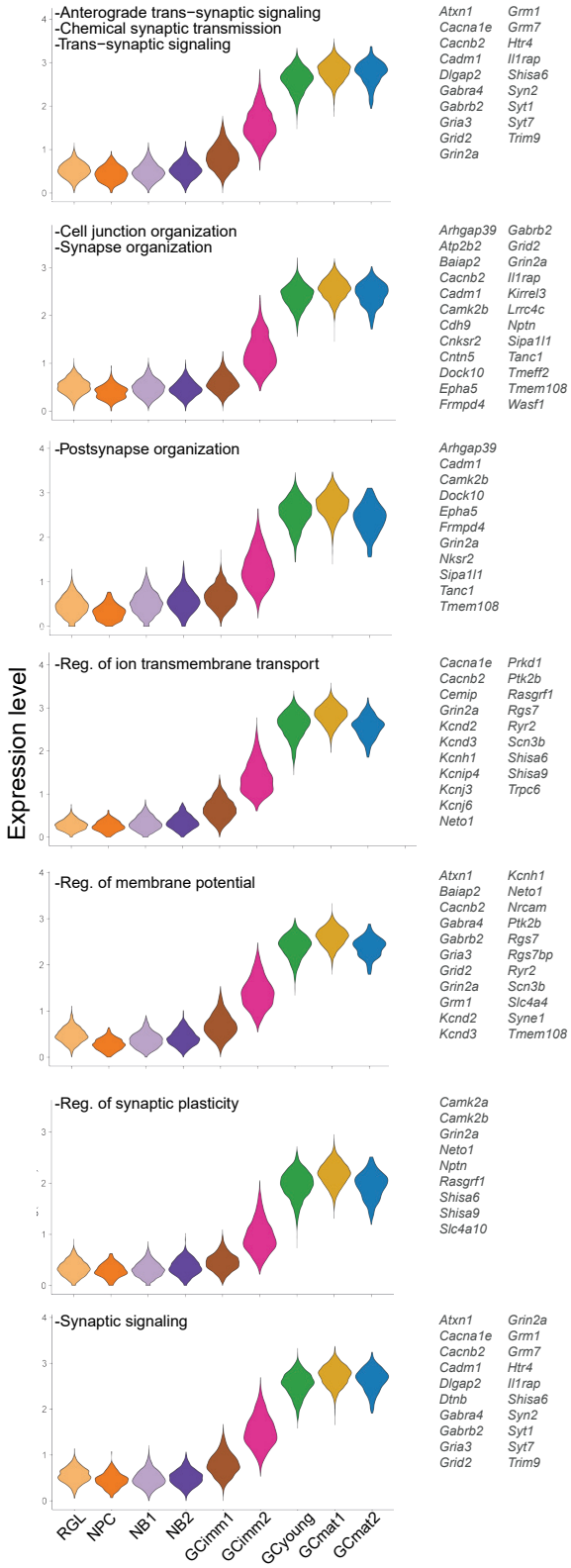

Figure S6

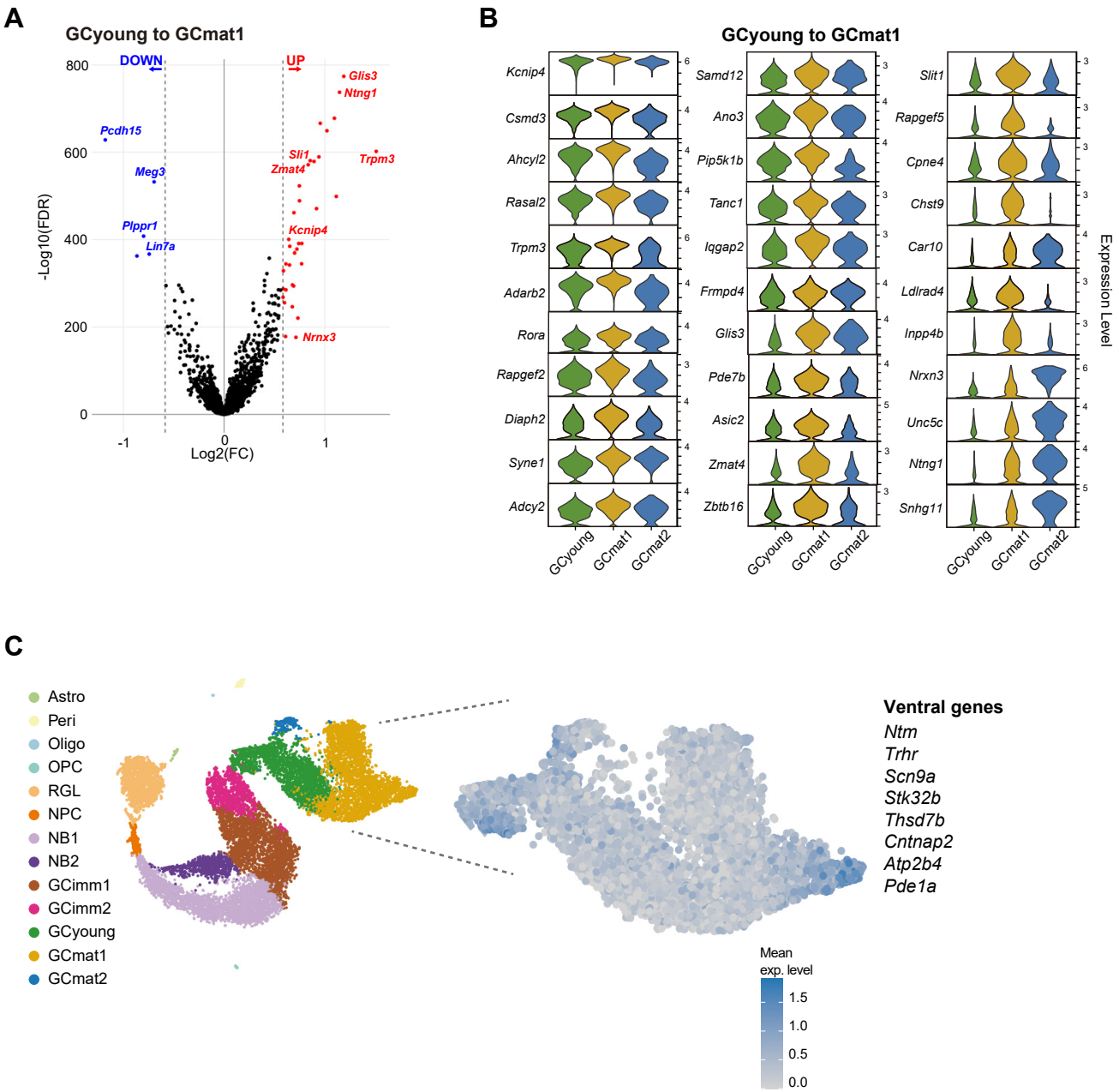
A
GCyoung to GCmat1
DOWN
UP
Glis3
Ntng1
Pcdh15
Sli1
Trpm3
Zmat4
Meg3
Plppr1
Kcnip4
Lin7a
Nrnx3
-Log10(FDR)
Log2(FC)
B
GCyoung to GCmat1
Kcnip4
Csmd3
Ahcyl2
Rasal2
Trpm3
Adarb2
Rora
Rapgef2
Diaph2
Syne1
Adcy2
Samd12
Ano3
Pip5k1b
Tanc1
Iqgap2
Frmpd4
Glis3
Pde7b
Asic2
Zmat4
Zbtb16
Slit1
Rapgef5
Cpne4
Chst9
Car10
Ldlrad4
Inpp4b
Nrxn3
Unc5c
Ntng1
Snhg11
GCyoung
GCmat1
GCmat2
Expression Level
C
Astro
Peri
Oligo
OPC
RGL
NPC
NB1
NB2
GCimm1
GCimm2
GCyoung
GCmat1
GCmat2
Ventral genes
Ntm
Trhr
Scn9a
Stk32b
Thsd7b
Cntnap2
Atp2b4
Pde1a
Mean exp. level
1.5
1.0
0.5
0.0

Figure S7

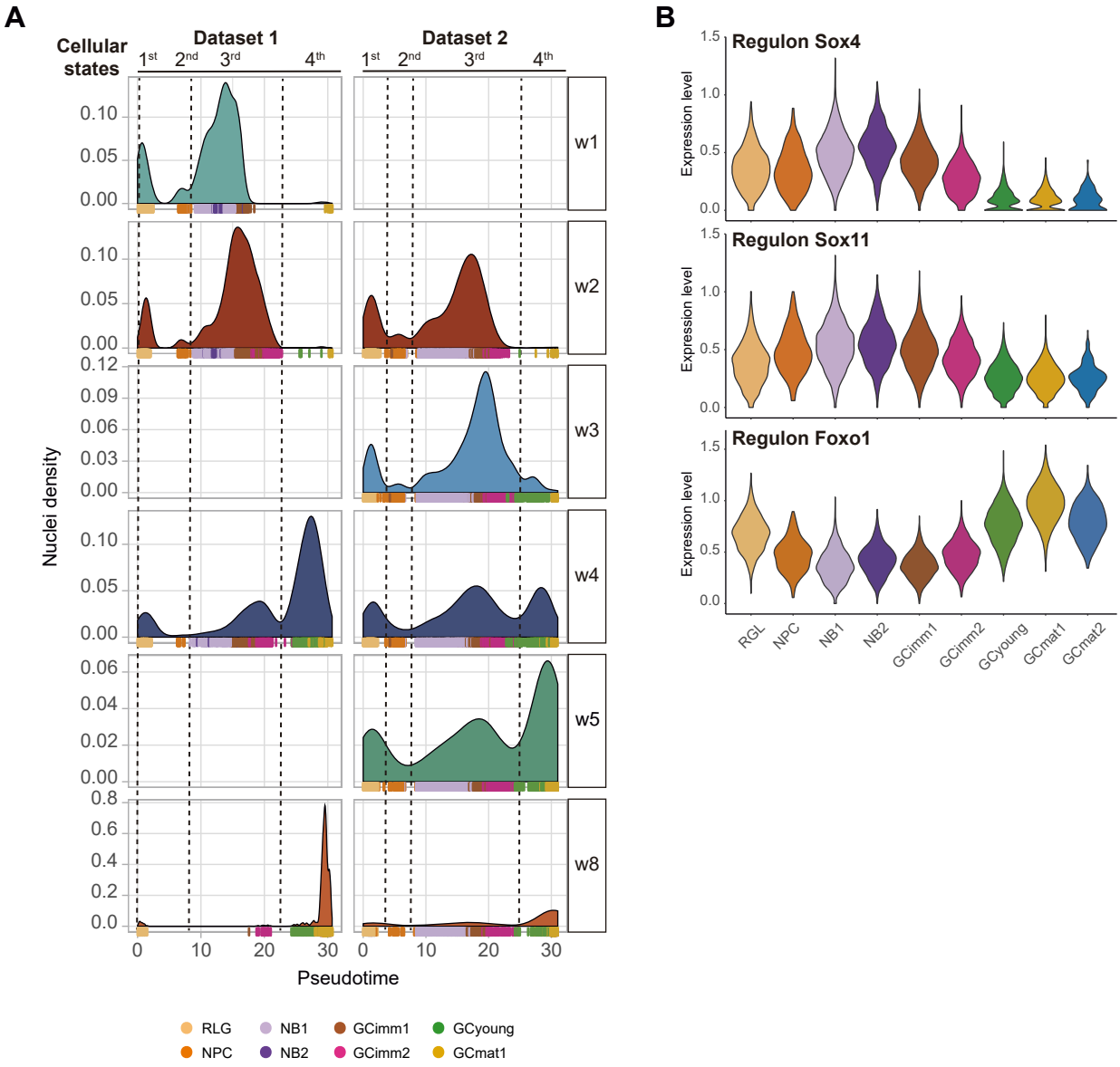
A
Cellular states
Dataset 1
Dataset 2
1st 2nd 3rd 4th
w1
w2
w3
w4
w5
w8
Nuclei density
Pseudotime
RLG
NPC
NB1
NB2
GCimm1
GCimm2
GCyoung
GCmat1
B
Regulon Sox4
Regulon Sox11
Regulon Foxo1
Expression level
RGL
NPC
NB1
NB2
GCimm1
GCimm2
GCyoung
GCmat1
GCmat2

Figure S8